MITSUBISHI ELECTRIC RESEARCH LABORATORIES
https://www.merl.com

Electric Satellite Station Keeping, Attitude Control, and Momentum Management by MPC

Caverly, Ryan; Di Cairano, Stefano; Weiss, Avishai

TR2020-153 December 02, 2020

Abstract

We propose a model predictive control (MPC) policy for simultaneous station keeping, attitude control, and momentum management of a low-thrust nadir-pointing geostationary satellite equipped with reaction wheels and on-off electric thrusters mounted on boom assemblies. Attitude control is performed using an inner-loop SO(3)-based control law with the reaction wheels, while the outer-loop MPC policy maintains the satellite within a narrow station keeping window and performs momentum management using electric thrusters. For reducing propellant consumption, our MPC uses two different prediction horizons: a short horizon for the states associated with the orbit's inclination and a longer horizon for all other states. Furthermore, to handle the on-off nature of the thruster while retaining low computational burden, we develop a strategy for quantizing the continuous thrust command, which also allows for trading off the number thrust pulses and fuel consumption. We validate the controller in a closed-loop simulation with the high-precision orbit propagation provided by the Systems Tool Kit (STK), and assess the robustness to model uncertainty and measurement noise.

IEEE Transactions on Control Systems Technology

Mitsubishi Electric Research Laboratories, Inc.
201 Broadway, Cambridge, Massachusetts 02139

Electric Satellite Station Keeping, Attitude Control, and Momentum Management by MPC

Ryan J. Caverly, *Member, IEEE,* Stefano Di Cairano, *Member, IEEE,* and Avishai Weiss, *Member, IEEE*

***Abstract*—We propose a model predictive control (MPC) policy for simultaneous station keeping, attitude control, and momentum management of a low-thrust nadir-pointing geostationary satellite equipped with reaction wheels and on-off electric thrusters mounted on boom assemblies. Attitude control is performed using an inner-loop $\mathrm{SO}(3)$-based control law with the reaction wheels, while the outer-loop MPC policy maintains the satellite within a narrow station keeping window and performs momentum management using electric thrusters. For reducing propellant consumption, our MPC uses two different prediction horizons: a short horizon for the states associated with the orbit's inclination and a longer horizon for all other states. Furthermore, to handle the on-off nature of the thruster while retaining low computational burden, we develop a strategy for quantizing the continuous thrust command, which also allows for trading off the number thrust pulses and fuel consumption. We validate the controller in a closed-loop simulation with the high-precision orbit propagation provided by the Systems Tool Kit (STK), and assess the robustness to model uncertainty and measurement noise.**

I. Introduction

Satellites in geostationary Earth orbit (GEO) have traditionally used chemical propulsion for station keeping maneuvers. Due to long GEO satellite lifetimes of twelve to fifteen years, electric propulsion [1–3], a more fuel efficient alternative to chemical propulsion, has recently become widely deployed on modern satellites [4]. Electric thrusters have significantly higher specific impulse than conventional chemical thrusters, meaning that they generate force more efficiently with respect to propellant mass, and can therefore be used to increase spacecraft longevity, and/or increase payloads, and/or decrease the cost of orbital insertion [5]. Conversely, high-efficiency electric thrusters produce only a fraction of the thrust of chemical propulsion systems. For station keeping applications in GEO, the magnitude of the thrust capabilities of the electric propulsion system are approximately the same magnitude as the perturbation forces acting on the satellite [6]. Thus, near-continuous operation of the electric propulsion system is required to counteract orbital perturbation-induced drift, posing new control challenges in their application. Whereas conventional chemical thrusters may be fired open-loop once every two weeks to compensate for GEO satellite drift [7], the near-continuous operation of electric thrusters suggests the use of closed-loop feedback control. As a result, a number of novel autonomous feedback control strategies for electric propulsion have been proposed in recent years [8–20].

In addition to station keeping, the lower thrust magnitude of electric propulsion systems enables their dual use in unloading momentum stored in a satellite's reaction wheels. Utilizing the same set of thrusters for both station keeping and momentum management eliminates the need for reaction control system thrusters, simplifying the propulsion design and reducing satellite weight. When the same set of thrusters are used for both station keeping and momentum management, they must be able to impart both forces and torques on the satellite. However, in many propulsion designs there are not enough thrusters to generate either pure forces or pure torques. For example, when considering a realistic thruster arrangement with gimbaled thrusters located on the satellite's anti-nadir face [21–23], any thruster torque simultaneously creates a net body force. This effect couples the typically decoupled orbital and attitude dynamics. As with station keeping, conventional momentum unloading is often a manually (open-loop) controlled operation [24–26]. However, with the additional difficulties associated with the dynamic coupling induced by the thrusters and the low thrust magnitude of the propulsion system, manual operation of both momentum unloading and station keeping, e.g. [27–31], may no longer be appropriate., and advanced control approaches may be necessary.

Model predictive control (MPC) is a receding horizon control strategy that exploits a prediction model of the system dynamics in order to attain a trajectory that minimizes a cost function, possibly accounting for several control objectives, subject to both state and control constraints over a finite future prediction horizon [32]. MPC is well suited for simultaneous station keeping and momentum management as it allows for fuel-efficiency maximization, has the ability to meet tight SK window and attitude error requirements, as well as stringent constraints on available thrust, and has the capacity to coordinate between coupled orbital and attitude control.

In [20] the authors have investigated the potential of using MPC for station-keeping, attitude control, and momentum management of electric propulsion GEO satellites. The MPC prediction model developed is based on the linearization of the satellite dynamics around their nominal operating condition. Euler angles are used to represent the attitude of the satellite relative to the nadir-pointing local-vertical, local-horizontal (LVLH) frame, and the Clohessy-Wiltshire Hill (CWH) equations are used for the satellite's position and velocity relative to a target location in GEO. The MPC policy enforces constraints relating to the size of the SK window, the

R. J. Caverly is with the Department of Aerospace Engineering and Mechanics, University of Minnesota, Minneapolis, MN 55455, USA. Email: rcaverly@umn.edu. He was an intern at MERL during the development of this work.

S. Di Cairano and A. Weiss are with Mitsubishi Research Laboratories, Cambridge, MA 02139, USA. Emails: {dicairano,weiss}@merl.com.

maximum allowed satellite attitude error, and the limits on thrust magnitude. To handle perturbation forces, a predicted disturbance sequence is incorporated into the MPC model based on analytic expressions for such forces, which increases the fuel efficiency.

While obtaining positive results in terms of control performance and propellant usage, [20] requires the use of 12 propulsion modulating thrusters that result in high cost and difficult implementation and packaging. Thus, here we develop a control architecture for a realistic thruster configuration. Specifically, we consider only 4 thrusters placed on the anti-nadir face of the satellite, which is usually free of equipment and solar panels. The thrusters are gimbaled in order to be able to produce pure forces, and forces and torques, as necessary for both station keeping and momentum management. Through several preliminary investigations, see, e.g., [33], [34] we selected a configuration where the thrusters are mounted on a boom assembly similar to [35]. As compared to placing thrusters directly on the satellite's anti-nadir face [33], this configuration achieves larger torque-free angles, i.e., the angles to thrust through the satellite's center of mass, which limits the thrust in the orbit radial direction that is not useful for control. Furthermore, the boom configuration achieves a wider thruster range of motion without risk of plume impingement on North-South mounted solar panels. As "North-South" Station-Keeping (NSSK), i.e. thrusting in the out-of-plane direction, is dominant in fuel consumption, these two are expected to result in improved fuel efficiency.

On the other hand the location, the number, and the on-off nature of the thrusters provide significant challenges for the control policy that require several changes from the one in [20]. First of all, due to the difference in the time scales between attitude control and station keeping and momentum management, to robustly achieve all the specifications we implement an inner-outer control architecture where an inner-loop $\mathrm{SO}(3)$-based controller regulates the attitude, and the outer-loop MPC controls the orbit and the momentum stored in the reaction wheels, also exploiting a closed-loop model of the attitude dynamics. Second, for reducing *delta-v*, a fuel efficiency measure that is independent of satellite mass and thruster efficiency, we propose a split-horizon MPC policy. In fact, while [5] claims that for a positional accuracy of 0.05–0.1 degrees, in the ideal case 41–51 m/s/year will be needed for NSSK depending on the epoch, the single-horizon MPC policy in [20] restricted to only 4 nadir-mounted thrusters uses about 59 m/s/year [34]. As it will be discussed later, the North-South delta-v decreases with decreasing horizon, and hence the split-horizon MPC policy uses a *shorter* prediction horizon for the states associated with the orbit's inclination. This result in a significant improvement of delta-v, close to the ideal case reported in [5]. Finally, we handle the on-off nature of the thrusters by developing a quantization scheme that also allows for calibrating the trade-off between and the thruster cycles, and hence the useful life of the thrusters, and the delta-v.

Even if some advanced electric propulsion systems can throttle thrust [36], many electric propulsion systems only operate at full magnitude, that is, by pulsing on and off, where here a pulse is to be interpreted as an on-off cycle of the thruster of any duration, i.e., not an impulse. The quantization can be incorporated directly within the control policy [9], which however results in solving mixed-integer linear programs (MILPs), which are computationally expensive and difficult to implement in real time, especially onboard of the satellite. Even if executed on ground stations, MILP solvers with good performance usually have fairly complicated code, and hence are hard and time consuming to certify. A more accessible approach is to compute continuous thrust commands and implement a quantization scheme to transform the continuous thrust commands into on-off thrust commands [14–16], [34] with limited impact on the system performance. Although PWM quantized control policies are capable of yielding very similar delta-v to non-quantized cases, they require a large number of on-off thruster pulses, see, e.g., [14–16], [34]. These approaches often achieve up to 30 pulses per electric thruster per orbit, which results in approximately $160,000$ on-off pulses per thruster over a typical 15 year satellite lifespan and that is an order of magnitude more than what allowed by current technology [37].

Thus, for quantizing the command signal with a number of cycles that is reasonable for the spacecraft life cycle, we propose a single-pulse quantization strategy with a feedback period that may be larger than the controller time step. The single on-off thrust pulse is selected by solving for the on and off thrust switching times that minimize the predicted state error induced by quantization, hence minimizing the deviation of the quantized policy from the non-quantized MPC policy.

The control architecture proposed in this paper is validated using Systems Tool Kit (STK)/Astrogator®, a high-fidelity orbit propagator in order to validate both our nonlinear model and the applicability of our MPC design to real-world implementation. In our simulations, we close the loop between the MPC policy and the STK/Astrogator propagator where, during each sampling period, the MPC policy computes the control commands and sends them to the STK propagator, which uses them to update the orbital position and returns the new satellite conditions to the controller for use during the next sampling period. In parallel, the attitude of the satellite is simulated by the continuous nonlinear differential equations for the reaction wheels torques commanded by the inner-loop controller and gimbaled thrusters torques commanded by MPC.

Following the presentation of some preliminaries and notation in this section, the paper proceeds[1] in Section II with a description of the satellite model considered in this paper. Section III describes the proposed MPC formulation, including the form of the inner-loop attitude controller, the closed-loop linearized satellite model, the split-horizon MPC policy, and the single-pulse thruster quantization scheme. Results of simulations performed with STK are presented in Section IV

[1]The propulsion and control architecture developed in this paper evolved through several preliminary results [33], [34], [38], [39]. This paper provides the final implementation that integrates all the effective elements discovered in such preliminary investigations, while providing a much more detailed discussion on the split-horizon MPC policy and the single-pulse quantization scheme, validates the system in simulations with the high-precision orbit propagation provided by STK, analyzes the effect of variations in several parameters of the quantization scheme and assess in simulation the robustness of the MPC policy to model uncertainties and measurement noise.

and simulations assessing the robustness of the MPC policy to different types of disturbances and error sources are performed in Section V-B. Concluding remarks are given in Section VI.

A. Preliminaries and Notation

The following notation is used throughout the paper. A reference frame $\mathcal{F}_a$ is defined by a set of three orthonormal dextral basis vectors, $\{\underrightarrow{a}^1, \underrightarrow{a}^2, \underrightarrow{a}^3\}$. An arbitrary physical vector, denoted as $\underrightarrow{v}$, is resolved in $\mathcal{F}_a$ as $\mathbf{v}_a$, where $\mathbf{v}_a^\mathsf{T} = \begin{bmatrix} v_{a1} & v_{a2} & v_{a3} \end{bmatrix}$ and $\underrightarrow{v} = v_{a1}\underrightarrow{a}^1 + v_{a2}\underrightarrow{a}^2 + v_{a3}\underrightarrow{a}^3$. The mapping between a physical vector resolved in different reference frames is given by the direction cosine matrix (DCM) $\mathbf{C}_{ba} \in \mathrm{SO}(3)$, where $\mathrm{SO}(3) = \{\mathbf{C} \in \mathbb{R}^{3\times 3} \,|\, \mathbf{C}^\mathsf{T}\mathbf{C} = \mathbf{1}, \det(\mathbf{C}) = +1\}$ and $\mathbf{1}$ is the identity matrix. For example, $\mathbf{v}_b = \mathbf{C}_{ba}\mathbf{v}_a$, where $\mathbf{v}_b$ is $\underrightarrow{v}$ resolved in $\mathcal{F}_b$ and $\mathbf{C}_{ba}$ represents the attitude of $\mathcal{F}_b$ relative to $\mathcal{F}_a$. Principle rotations about the $\underrightarrow{a}^i$ axis by an angle α are denoted as $\mathbf{C}_{ba} = \mathbf{C}_i(\alpha)$. The cross, uncross, and anti-symmetric projection operators used throughout this paper are defined as follows. The cross operator, $(\cdot)^\times : \mathbb{R}^3 \to \mathfrak{so}(3)$, is defined as

$$\mathbf{a}^\times = -\mathbf{a}^{\times^\mathsf{T}} = \begin{bmatrix} 0 & -a_3 & a_2 \\ a_3 & 0 & -a_1 \\ -a_2 & a_1 & 0 \end{bmatrix},$$

where $\mathbf{a}^\mathsf{T} = \begin{bmatrix} a_1 & a_2 & a_3 \end{bmatrix}$ and $\mathfrak{so}(3) = \{\mathbf{S} \in \mathbb{R}^{3\times 3} \,|\, \mathbf{S} + \mathbf{S}^\mathsf{T} = \mathbf{0}\}$. The uncross operator, $(\cdot)^\vee : \mathfrak{so}(3) \to \mathbb{R}^3$, is defined as $\mathbf{A}^\vee = \begin{bmatrix} a_1 & a_2 & a_3 \end{bmatrix}^\mathsf{T}$, where $\mathbf{A} = \mathbf{a}^\times$. The anti-symmetric projection operator $\mathcal{P}_a(\cdot) : \mathbb{R}^{3\times 3} \to \mathfrak{so}(3)$, is given by $\mathcal{P}_a(\mathbf{U}) = \frac{1}{2}\left(\mathbf{U} - \mathbf{U}^\mathsf{T}\right)$, for all $\mathbf{U} \in \mathbb{R}^{3\times 3}$. The physical vector describing the position of a point p relative to a point q is given by $\underrightarrow{r}^{pq}$. Similarly, the angular velocity of $\mathcal{F}_b$ relative to $\mathcal{F}_a$ is given by $\underrightarrow{\omega}^{ba}$. In Section V-B, quantities that are uncertain or feature measurement noise are denoted with a tilde, (e.g., $\tilde{\mathbf{v}}_a$ is a noisy measurement of $\mathbf{v}_a$).

II. Problem Statement and Spacecraft Model

Consider the satellite shown in Fig. 2, which consists of a rigid bus equipped with three axisymmetric reaction wheels and four electric thrusters mounted on gimbaled booms. The satellite is nominally in a circular GEO orbit.

A. Control Objectives

The control objectives considered in this work are to 1) minimize fuel consumption and 2) reduce the number of on-off thruster pulses, while ensuring that

a) the satellite is maintained within the prescribed station-keeping window,
b) a nadir-pointing attitude is maintained within a prescribed tolerance,
c) angular momentum stored in the reaction wheels is unloaded, and
d) the limitations of the thrusters (e.g., thrust magnitude, boom gimbal angle limits, power limitations) are enforced.

B. Satellite Model

The Earth-centered inertial (ECI) frame is defined as $\mathcal{F}_g$. The reference frame $\mathcal{F}_p$ is aligned with the spacecraft bus, where nominally $\underrightarrow{p}^1$ points towards the Earth and $\underrightarrow{p}^2$ points North. The angular velocity of $\mathcal{F}_p$ relative to $\mathcal{F}_g$ is $\underrightarrow{\omega}^{pg}$ and the DCM describing the attitude of the spacecraft (i.e., $\mathcal{F}_p$) relative to $\mathcal{F}_g$ is $\mathbf{C}_{pg}$. The center of mass of the spacecraft is denoted by point c in Fig. 2(a). The position of the spacecraft center of mass relative to a point w at the center of the Earth is given by $\underrightarrow{r}^{cw}$. The equations of motion of the satellite are

$$\ddot{\mathbf{r}}_g^{cw} = -\mu \frac{\mathbf{r}_g^{cw}}{\left\|\mathbf{r}_g^{cw}\right\|^3} + \mathbf{a}_g^p + \frac{1}{m_\mathcal{B}}\mathbf{C}_{pg}^\mathsf{T}\mathbf{f}_p^{\text{thrust}}, \tag{1a}$$

$$\mathbf{J}_p^{\mathcal{B}c}\dot{\boldsymbol{\omega}}_p^{pg} = -\boldsymbol{\omega}_p^{pg^\times}\left(\mathbf{J}_p^{\mathcal{B}c}\boldsymbol{\omega}_p^{pg} + \mathbf{J}_s\boldsymbol{\nu}\right) - \mathbf{J}_s\boldsymbol{\eta} + \boldsymbol{\tau}_p^p + \boldsymbol{\tau}_p^{\text{thrust}}, \tag{1b}$$

$$\dot{\mathbf{C}}_{pg} = -\boldsymbol{\omega}_p^{pg^\times}\mathbf{C}_{pg}, \tag{1c}$$

$$\dot{\boldsymbol{\nu}} = \boldsymbol{\eta}, \tag{1d}$$

where $m_\mathcal{B}$ is the mass of the spacecraft, $\mathbf{J}_p^{\mathcal{B}c}$ is the moment of inertia of the spacecraft relative to point c and resolved in $\mathcal{F}_p$, $\boldsymbol{\nu}^\mathsf{T} = \begin{bmatrix} \nu_1 & \nu_2 & \nu_3 \end{bmatrix}$ are the reaction wheel angular rates, $\boldsymbol{\eta}$ is the angular acceleration of the reaction wheels, $\mathbf{J}_s$ is the moment of inertia of the reaction wheel array, $\mathbf{f}_p^{\text{thrust}}$ is the force produced by the thrusters, $\boldsymbol{\tau}_p^{\text{thrust}}$ is the torque produced by the thrusters. The term $\mathbf{a}_g^p$ represents the external perturbations on the satellite. For satellites in GEO, the main perturbations are solar and lunar gravitational attraction, which induce a drift in orbital inclination; solar radiation pressure (SRP), which affects orbit eccentricity; and the anisotropic geopotential, that is, Earth's non-spherical gravitational field, which induces in-orbital-plane longitudinal drift [31],[40, Ch. 7]. Analytic expressions for these are given in [20, Eq. (10)]. Figure 1 shows an annual time history of the disturbance force components for a 4000kg satellite in GEO. The term $\boldsymbol{\tau}_p^p$ represents the SRP perturbation torque, which assumes total absorption, and is given by [41, p. 229].

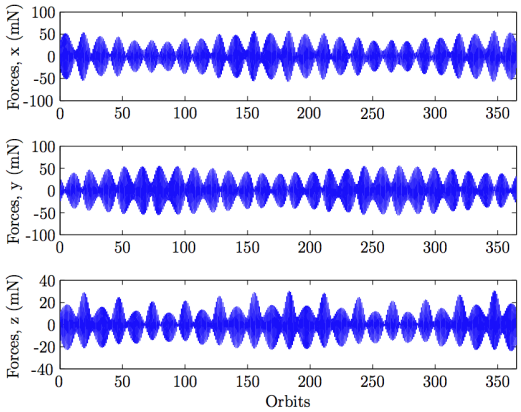

Fig. 1. Annual disturbance force components

The thruster configuration is illustrated in Fig. 2, where four electric thrusters are mounted on two boom-thruster assemblies, one of which nominally points North, while the

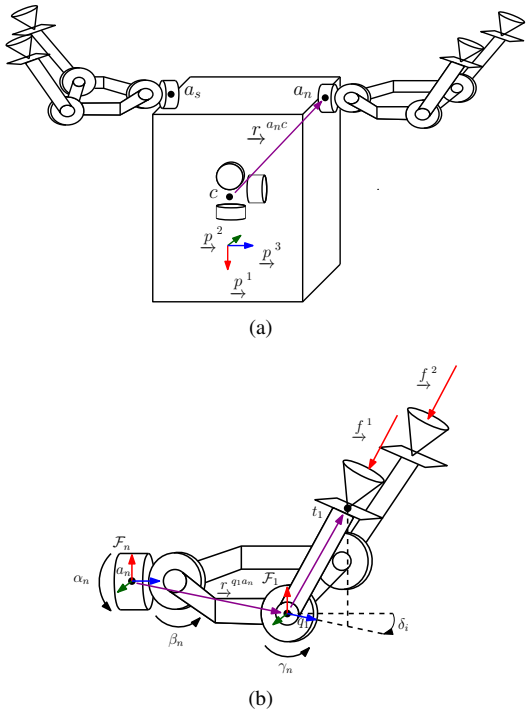

Fig. 2. Schematic of (a) the spacecraft including three axisymmetric reaction wheels and four electric thrusters, and (b) the North-facing boom-thruster assembly.

other nominally points South. A detailed view of the North-facing boom-thruster assembly is provided in Fig. 2(b). Each assembly has two fixed gimbal angles, $\bar{\alpha}_a$ and $\bar{\beta}_a$, $a \in \{n, s\}$, as well as an actuated gimbal angle γ_a, $a \in \{n, s\}$. The subscripts n and s refer to the gimbal angles associated with the North-facing assembly and the South-facing assembly, respectively. The position of the actuated gimbal of thruster i relative to the spacecraft center of mass is $\underrightarrow{r}^{q_i c}$. The thrusters are canted by fixed angles δ_i, $i = 1, 2, 3, 4$, such that for a nominal gimbal angle $\bar{\gamma}_a$, $a \in \{n, s\}$, each thruster fires through the center of mass of the spacecraft. The force vector produced by thruster i is $\underrightarrow{f}^{i}$, and can be resolved in $\mathcal{F}_p$ as

$$\mathbf{f}_p^i = -f^i \mathbf{C}_{ip}^{\mathsf{T}} \mathbf{C}_2(\gamma_a) \mathbf{1}_3, \tag{2}$$

where $f^i = \left| \underrightarrow{f}^{i} \right|$ is the thrust magnitude, $\mathbf{1}_3 = \begin{bmatrix} 0 & 0 & 1 \end{bmatrix}^{\mathsf{T}}$, $\mathbf{C}_{ip} = \mathbf{C}_{ia}\mathbf{C}_{ap}$, $\mathbf{C}_{ia} = \mathbf{C}_1(\delta_i)\mathbf{C}_2(\bar{\beta}_i)\mathbf{C}_3(\bar{\alpha}_a)$, $\mathbf{C}_{np} = \mathbf{C}_3(\pi)$, and $\mathbf{C}_{sp} = \mathbf{C}_1(\pi)\mathbf{C}_3(\pi)$. The torque generated by the thruster on the spacecraft is given by

$$\boldsymbol{\tau}_p^i = \mathbf{r}_p^{q_i c^\times} \mathbf{f}_p^i. \tag{3}$$

The net force and torque applied to the spacecraft by the four thrusters can be written as

$$\mathbf{f}_p^{\text{thrust}} = \sum_{i=1}^{4} \mathbf{B}_i^f \mathbf{u}_i, \tag{4}$$

and

$$\boldsymbol{\tau}_p^{\text{thrust}} = \sum_{i=1}^{4} \mathbf{r}_p^{q_i c^\times} \mathbf{B}_i^\tau \mathbf{u}_i, \tag{5}$$

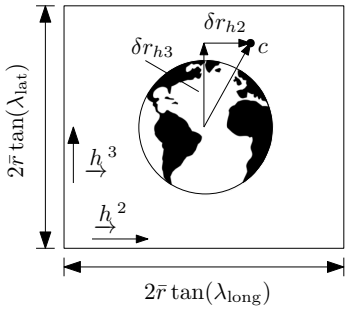

Fig. 3. Illustration of the station keeping window described by $-\bar{r}\tan(\lambda_{\text{long}}) \leq \delta r_{h2} \leq \bar{r}\tan(\lambda_{\text{long}})$ and $-\bar{r}\tan(\lambda_{\text{lat}}) \leq \delta r_{h3} \leq \bar{r}\tan(\lambda_{\text{lat}})$, with the view looking in the $-\underrightarrow{h}^1$ direction towards Earth. The point c denotes the spacecraft's center of mass.

with $\mathbf{u}_i^{\mathsf{T}} = \begin{bmatrix} \sin(\gamma_a) f^i & \cos(\gamma_a) f^i \end{bmatrix}$ and constant matrices

$$\mathbf{B}_i^f = \mathbf{C}_{ip}^{\mathsf{T}} \begin{bmatrix} -1 & 0 \\ 0 & 0 \\ 0 & -1 \end{bmatrix}, \quad \mathbf{B}_i^\tau = \mathbf{r}_p^{q_i c^\times} \mathbf{B}_i^f.$$

C. Station Keeping Window

For the purposes of station keeping and for linearizing the spacecraft's equations of motion, it is useful to express the spacecraft's position relative to the desired nominal circular GEO orbit. To this end, Hill's frame, denoted by $\mathcal{F}_h$, is defined by basis vectors $\underrightarrow{h}^1$ aligned with the orbital radius and $\underrightarrow{h}^3$ orthogonal to the orbital plane. The position of the spacecraft center of mass relative to a point w at the center of the Earth, resolved in $\mathcal{F}_h$ is given by $\mathbf{r}_h^{cw}$. Defining the satellite's nominal position in a circular orbit resolved in $\mathcal{F}_g$ as $\bar{\mathbf{r}}_g$, yields the position error of the spacecraft

$$\delta \mathbf{r}_h = \begin{bmatrix} \delta r_{h1} & \delta r_{h2} & \delta r_{h3} \end{bmatrix}^{\mathsf{T}} = \mathbf{r}_h^{cw} - \mathbf{C}_{hg} \bar{\mathbf{r}}_g. \tag{6}$$

The station keeping window is given by [7, Ch. 5]

$$\begin{aligned} -\bar{r}\tan(\lambda_{\text{long}}) \leq \delta r_{h2} \leq \bar{r}\tan(\lambda_{\text{long}}), \\ -\bar{r}\tan(\lambda_{\text{lat}}) \leq \delta r_{h3} \leq \bar{r}\tan(\lambda_{\text{lat}}), \end{aligned} \tag{7}$$

where $\bar{r} = \|\bar{\mathbf{r}}_g\|$, and λ_{long} and λ_{lat} are the maximum deviations in longitude and latitude, respectively, that define the station keeping window. An illustration of the station keeping window is shown in Fig. 3. Although no single component of $\delta \mathbf{r}_h$ exactly captures the inclination i of the satellite's orbit relative to the desired geostationary orbit, for small deviations from the center of the station keeping window, the coordinate δr_{h3} is a good surrogate for the inclination. The inclination of the orbit can be approximated as $\sin(i) \approx \delta r_{h3} / \|\delta \mathbf{r}_h\|$. For small inclination angles, which is the case here since the station keeping window is small compared to the geostationary orbit radius, this becomes $i \approx \delta r_{h3} / \|\delta \mathbf{r}_h\|$. This approximation is relevant in the split-horizon MPC policy presented in Section III-D, where the states δr_{h3}^{cw} and $\delta \dot{r}_{h3}^{cw}$ use a different prediction horizon than the rest of the system states.

III. MPC Formulation

Next, we describe the control architecture that includes an inner-loop controller commanding the reaction wheels to

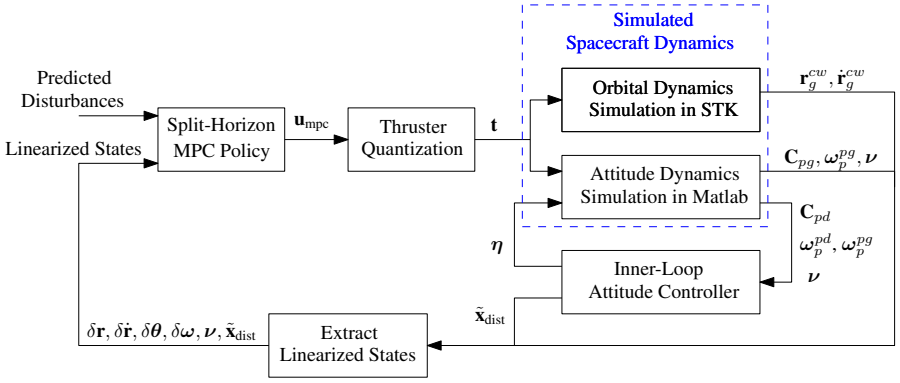

Fig. 4. Block diagram of the proposed control architecture, including the simulation model used in Section IV for assessing the closed-loop performance.

control the attitude, a split horizon MPC policy that commands the thrusters to perform station keeping and momentum management based on the prediction model of the satellite in closed-loop with the inner-loop controller, and a quantization scheme that controls the on-off behavior of the thrusters based on the commands issued by MPC and the limitations of the propulsion system.

A. Inner-Loop Attitude Controller

The reaction wheels are directly actuated by the spacecraft attitude controller, which is seen as an inner-loop controller by the MPC policy. The disturbance torque is modeled as described by the LTI system

$$\begin{aligned} \dot{\mathbf{x}}_{\text{dist}} &= \mathbf{A}_{\text{dist}}\mathbf{x}_{\text{dist}}, \\ \boldsymbol{\tau}_p^p &= \mathbf{C}_{\text{dist}}\mathbf{x}_{\text{dist}}. \end{aligned} \tag{8}$$

and estimated by the observer

$$\begin{aligned} &\dot{\hat{\mathbf{x}}}_{\text{dist}} = \mathbf{A}_{\text{dist}}\hat{\mathbf{x}}_{\text{dist}} + \mathbf{B}_{\text{dist}}\mathbf{u}_{\text{dist}}, \quad \hat{\boldsymbol{\tau}}_p^p = \mathbf{C}_{\text{dist}}\hat{\mathbf{x}}_{\text{dist}}, \\ &\mathbf{u}_{\text{dist}} = \boldsymbol{\omega}_p^{pd} + \mathbf{K}_1\mathbf{S}, \quad \mathbf{S} = -\boldsymbol{\mathcal{P}}_a\left(\mathbf{C}_{pd}\right)^{\vee}, \end{aligned} \tag{9}$$

where $\hat{\boldsymbol{\tau}}_p^p$ is the estimate of $\boldsymbol{\tau}_p^p$, $\mathbf{K}_1 = \mathbf{K}_1^{\mathsf{T}} > 0$, $\mathbf{B}_{\text{dist}} = \mathbf{P}_{\text{dist}}^{-1}\mathbf{C}_{\text{dist}}^{\mathsf{T}}$ is designed such that $(\mathbf{A}_{\text{dist}}, \mathbf{B}_{\text{dist}}, \mathbf{C}_{\text{dist}})$ is positive real, and $\mathbf{P}_{\text{dist}} = \mathbf{P}_{\text{dist}}^{\mathsf{T}} > 0$ satisfies the Lyapunov equation $\mathbf{A}_{\text{dist}}^{\mathsf{T}}\mathbf{P}_{\text{dist}} + \mathbf{P}_{\text{dist}}\mathbf{A}_{\text{dist}} = -\mathbf{Q}_{\text{dist}}$, $\mathbf{Q}_{\text{dist}} = \mathbf{Q}_{\text{dist}}^{\mathsf{T}} \geq 0$. The attitude controller is [42]

$$\begin{aligned} \boldsymbol{\mu}_1 &= \boldsymbol{\omega}_p^{pg\times}\left(\mathbf{J}_p^{\mathcal{B}c}\boldsymbol{\omega}_p^{pg} + \mathbf{J}_s\boldsymbol{\nu}\right) - \mathbf{J}_p^{\mathcal{B}c}\left(\mathbf{K}_1\dot{\mathbf{S}} + \boldsymbol{\omega}_p^{pd\times}\boldsymbol{\omega}_p^{pg}\right), \\ \boldsymbol{\mu}_2 &= -\hat{\boldsymbol{\tau}}_p^p, \\ \boldsymbol{\mu}_3 &= -\mathbf{K}_\nu\left(\boldsymbol{\omega}_p^{pd} + \mathbf{K}_1\mathbf{S}\right) - \mathbf{K}_p\mathbf{S}, \end{aligned} \tag{10}$$

where $\mathbf{K}_\nu = \mathbf{K}_\nu^{\mathsf{T}} > 0$, $\mathbf{K}_p = \mathbf{K}_p^{\mathsf{T}} > 0$, and the attitude control input is $\boldsymbol{\eta} = -\mathbf{J}_s^{-1}\left(\boldsymbol{\mu}_1 + \boldsymbol{\mu}_2 + \boldsymbol{\mu}_3\right)$. See Figure 4 for a block diagram of the control architecture and how the inner-loop controller interfaces with the spacecraft dynamics and other components of the MPC policy.

B. Closed-Loop Linearized Model

The MPC policy prediction model is obtained by linearizing the spacecraft dynamics in closed-loop with the attitude controller about a nominal circular orbit with mean motion n, nadir-pointing attitude, zero reaction wheel speeds, and zero observer states. The closed-loop linearized equations of motion are

$$\begin{aligned} \delta\ddot{\mathbf{r}}_h &= -2\bar{\boldsymbol{\omega}}_p^{\times}\delta\dot{\mathbf{r}}_h - \boldsymbol{\Omega}\delta\mathbf{r}_h + \mathbf{a}_h^p + \frac{1}{m_{\mathcal{B}}}\mathbf{C}_{dh}^{\mathsf{T}}\mathbf{f}_p^{\text{thrust}}, \\ \delta\dot{\boldsymbol{\theta}} &= -\boldsymbol{\omega}_0^{\times}\delta\boldsymbol{\theta} + \delta\boldsymbol{\omega}, \\ \delta\dot{\boldsymbol{\omega}} &= \left(\left(\mathbf{K}_1 - \bar{\boldsymbol{\omega}}_p^{\times}\right)\bar{\boldsymbol{\omega}}_p^{\times} + \mathbf{J}_p^{\mathcal{B}c^{-1}}\left(\mathbf{K}_\nu\bar{\boldsymbol{\omega}}_p^{\times} - \mathbf{K}\right)\right)\delta\boldsymbol{\theta} \\ &\quad + \left(-\mathbf{K}_1 + \bar{\boldsymbol{\omega}}_p^{\times} - \mathbf{J}_p^{\mathcal{B}c^{-1}}\mathbf{K}_\nu\right)\delta\boldsymbol{\omega} \\ &\quad - \mathbf{J}_p^{\mathcal{B}c^{-1}}\mathbf{C}_{\text{dist}}\tilde{\mathbf{x}}_{\text{dist}} + \boldsymbol{\tau}_p^{\text{thrust}}, \\ \dot{\boldsymbol{\nu}} &= -\mathbf{J}_s^{-1}\left(\mathbf{J}_p^{\mathcal{B}c}\left(\mathbf{K}_1 - \bar{\boldsymbol{\omega}}_p^{\times}\right)\bar{\boldsymbol{\omega}}_p^{\times} + \mathbf{K}_\nu\bar{\boldsymbol{\omega}}_p^{\times} - \mathbf{K}\right)\delta\boldsymbol{\theta} \\ &\quad -\mathbf{J}_s^{-1}\Big(\mathbf{J}_p^{\mathcal{B}c}\left(-\mathbf{K}_1 + \bar{\boldsymbol{\omega}}_p^{\times}\right) - \mathbf{K}_\nu + \bar{\boldsymbol{\omega}}_p^{\times}\mathbf{J}_p^{\mathcal{B}c} \\ &\quad - \left(\mathbf{J}_p^{\mathcal{B}c}\bar{\boldsymbol{\omega}}_p\right)^{\times}\Big)\delta\boldsymbol{\omega} - \mathbf{J}_s^{-1}\bar{\boldsymbol{\omega}}_p^{\times}\mathbf{J}_s\boldsymbol{\nu} + \mathbf{J}_s^{-1}\mathbf{C}_{\text{dist}}\tilde{\mathbf{x}}_{\text{dist}}, \\ \dot{\tilde{\mathbf{x}}}_{\text{dist}} &= \mathbf{A}_{\text{dist}}\tilde{\mathbf{x}}_{\text{dist}} + \mathbf{B}_{\text{dist}}\delta\boldsymbol{\omega} + \mathbf{B}_{\text{dist}}\left(\mathbf{K}_1 - \bar{\boldsymbol{\omega}}_p^{\times}\right)\delta\boldsymbol{\theta}, \end{aligned} \tag{11}$$

where $\bar{\boldsymbol{\omega}}_p^{\mathsf{T}} = \begin{bmatrix} 0 & 0 & n \end{bmatrix}$, $\mathbf{C}_{pd} = \mathbf{C}_{pg}\mathbf{C}_{dg}^{\mathsf{T}}$ is the attitude error between $\mathbf{C}_{pg}$ and the desired nadir-pointing orientation $\mathbf{C}_{dg}$, $\mathbf{C}_{pg}$ is parameterized by a $3-2-1$ Euler angle sequence with angles $\delta\boldsymbol{\theta}^{\mathsf{T}} = \begin{bmatrix} \delta\phi & \delta\theta & \delta\psi \end{bmatrix}$, $\mathbf{K} = \mathbf{K}_\nu\mathbf{K}_1 + \mathbf{K}_p$, and $\boldsymbol{\Omega} = \text{diag}\{-3n^2, 0, n^2\}$. The closed-loop linearized model is written in state-space form as

$$\dot{\mathbf{x}} = \mathbf{A}\mathbf{x} + \mathbf{B}\mathbf{u} + \mathbf{B}_w\mathbf{w}, \tag{12}$$

where $\mathbf{x}^{\mathsf{T}} = \begin{bmatrix} \delta\mathbf{r}^{\mathsf{T}} & \delta\dot{\mathbf{r}}^{\mathsf{T}} & \delta\boldsymbol{\theta}^{\mathsf{T}} & \delta\boldsymbol{\omega}^{\mathsf{T}} & \boldsymbol{\nu}^{\mathsf{T}} & \tilde{\mathbf{x}}_{\text{dist}}^{\mathsf{T}} \end{bmatrix}$, $\mathbf{u}^{\mathsf{T}} = \begin{bmatrix} \mathbf{u}_1^{\mathsf{T}} & \mathbf{u}_2^{\mathsf{T}} & \mathbf{u}_3^{\mathsf{T}} & \mathbf{u}_4^{\mathsf{T}} \end{bmatrix}$, and $\mathbf{w}^{\mathsf{T}} = \begin{bmatrix} \mathbf{a}_h^{p^{\mathsf{T}}} & \mathbf{0} & \mathbf{0} & \mathbf{0} & \mathbf{0} & \mathbf{0} \end{bmatrix}$. The relationship between $\mathbf{u}$ and the terms $\mathbf{f}_p^{\text{thrust}}$ and $\boldsymbol{\tau}_p^{\text{thrust}}$ is given in (4) and (5). The discrete-time form of the closed-loop linearized model (12) with time step Δt is

$$\mathbf{x}_{k+1} = \mathbf{A}_{\text{d}}\mathbf{x}_k + \mathbf{B}_{\text{d}}\mathbf{u}_k + \mathbf{B}_{w,\text{d}}\mathbf{w}_k. \tag{13}$$

Equation (13) is used along a prediction horizon $k = 1, \ldots, N$. During the prediction horizon, the disturbances $\mathbf{w}_k, k = 1, \ldots, N$ can be approximated as the disturbances associated with the satellite at its desired position, since the satellite will be kept very close to the desired position during correct operation.

C. MPC Input and State Constraints

The magnitude of the force produced by each thruster must satisfy $\left\|\mathbf{f}_p^i\right\|_2 \leq f_{\max}$, where $f_{\max}$ is the maximum allowable

thrust. To reduce the computational burden, the quadratic constraint is conservatively approximated by linear constraint $\left\|\mathbf{f}_p^i\right\|_\infty \leq \frac{f_{\max}}{\sqrt{2}}$. Furthermore, the thrusters must fire away from the spacecraft bus, which is enforced by the constraint $\mathbf{f}_i^i \leq 0$. Thus, we impose the input constraints

$$\mathbf{u}_{\min} \leq \mathbf{u} \leq \mathbf{u}_{\max},\ \mathbf{u}_{\max} = \frac{f_{\max}}{\sqrt{2}}[1\ \ldots\ 1]^\mathsf{T},\ \mathbf{u}_{\min} = \mathbf{0}. \quad (14)$$

There is an additional physical constraint that the gimbal angle γ_n must be identical for the pair of inputs $\mathbf{u}_1$ and $\mathbf{u}_2$ at any time instant, since they share this angle. The same is true for γ_s with the pair of inputs $\mathbf{u}_3$ and $\mathbf{u}_4$. Based on our preliminary studies, this constraint is ignored in the MPC policy and is addressed in the quantization scheme in Section III-E.

The prescribed station keeping window and the maximum allowable attitude error are enforced as state constraints. Since the closed-loop linearized orbital dynamics equation of motion is given in Hill's frame, the station keeping window constraint is formulated as

$$\delta\bar{\mathbf{r}}_{\min} \leq \delta\bar{\mathbf{r}} \leq \delta\bar{\mathbf{r}}_{\max}, \qquad \delta\boldsymbol{\theta}_{\min} \leq \delta\boldsymbol{\theta} \leq \delta\boldsymbol{\theta}_{\max}. \quad (15)$$

where $\delta\bar{\mathbf{r}}_{\min} = -\delta\bar{\mathbf{r}}_{\max}$, $\delta\bar{\mathbf{r}}_{\max} = [\infty\ \bar{r}\tan(\lambda_{\text{long}})\ \bar{r}\tan(\lambda_{\text{lat}})]^\mathsf{T}$, and $\delta\boldsymbol{\theta}_{\min} = -\delta\boldsymbol{\theta}_{\max}$.

D. Split-Horizon MPC Policy

The split-horizon MPC policy is

$$u(t) = \kappa_{\text{MPC}}(x(t)) = u^*_{0|t} \quad (16)$$

where $u^*_{k|t}$, $k = 0, \ldots N_2 - 1$ are the optimal control inputs computed by solving,

$$\begin{aligned}
\min_{\mathcal{U}_t}\ & \mathbf{x}_{N_1|t}^\mathsf{T}\mathbf{P}_1\mathbf{x}_{N_1|t} + \sum_{k=0}^{N_1-1}\left(\mathbf{x}_{k|t}^\mathsf{T}\mathbf{Q}\mathbf{x}_{k|t} + \mathbf{u}_{k|t}^\mathsf{T}\mathbf{R}\mathbf{u}_{k|t}\right) \\
& + \mathbf{x}_{N_2|t}^\mathsf{T}\mathbf{P}_2\mathbf{x}_{N_2|t} + \sum_{k=N_1}^{N_2-1}\left(\mathbf{x}_{k|t}^\mathsf{T}\mathbf{Q}_2\mathbf{x}_{k|t} + \mathbf{u}_{k|t}^\mathsf{T}\mathbf{R}\mathbf{u}_{k|t}\right) \\
\text{s.t.}\ & \mathbf{x}_{k+1|t} = \mathbf{A}_{\text{d}}\mathbf{x}_{k|t} + \mathbf{B}_{\text{d}}\mathbf{u}_{k|t} + \mathbf{B}_{w,\text{d}}\mathbf{w}_{k|t}, \\
& \mathbf{x}_{0|t} = \mathbf{x}(t),\ \mathbf{w}_{k|t} = \hat{\mathbf{w}}_t(t+k), \\
& \mathbf{x}_{\min} \leq \mathbf{x}_{k|t} \leq \mathbf{x}_{\max}, \quad 0 \leq k \leq N_1, \\
& \mathbf{x}_{\min,2} \leq \mathbf{x}_{k|t} \leq \mathbf{x}_{\max,2}, \quad N_1 < k \leq N_2, \\
& \mathbf{u}_{\min} \leq \mathbf{u}_{k|t} \leq \mathbf{u}_{\max}, \qquad (17)
\end{aligned}$$

where N_1 is the prediction horizon of the states δr_{h3}^{cw} and $\delta \dot{r}_{h3}^{cw}$, N_2 is the prediction horizon of the remaining states, $\mathcal{U}_t = \{\mathbf{u}_{0|t}, \ldots, \mathbf{u}_{N_2-1|t}\}$, $\mathbf{Q} = \mathbf{Q}^\mathsf{T} \geq 0$ and $\mathbf{R} = \mathbf{R}^\mathsf{T} > 0$ are constant state and control weighting matrices, and $\hat{\mathbf{w}}_i(j)$ is the open-loop predicted disturbance column matrix at time j based on data at time i. The matrix $\mathbf{Q}_2$ is the same as $\mathbf{Q}$, except the rows and columns associated with the states δr_{h3}^{cw} and $\delta \dot{r}_{h3}^{cw}$ are set to zero. The matrices $\mathbf{P}_1$ and $\mathbf{P}_2$ are constructed from the matrix $\mathbf{P} = \mathbf{P}^\mathsf{T} > 0$, which is the solution to the discrete-time algebraic Riccati equation. The matrix $\mathbf{P}_1$ contains the rows and columns of $\mathbf{P}$ associated with the states δr_{h3}^{cw} and $\delta \dot{r}_{h3}^{cw}$ and zeros the others, while $\mathbf{P}_2$ does the opposite, so that $\mathbf{P}_1 + \mathbf{P}_2 = \mathbf{P}$. This is possible since $\mathbf{P}$ is block-diagonal under a coordinate transformation that reorders the states such that δr_{h3}^{cw} and $\delta \dot{r}_{h3}^{cw}$ are at the end of the state column matrix. The state constraints $\mathbf{x}_{\min}$ and $\mathbf{x}_{\max}$ are based on the station keeping and attitude constraints. The bounds $\mathbf{x}_{\min,2}$, $\mathbf{x}_{\max,2}$ are identical to $\mathbf{x}_{\min}$, $\mathbf{x}_{\max}$, but the out-of-plane bounds

$$\begin{aligned}
\delta\mathbf{r}_{\min}^\mathsf{T} &= \begin{bmatrix}-\infty & -\bar{r}\tan(\lambda_{\text{long}}) & -\infty\end{bmatrix}, \\
\delta\mathbf{r}_{\max}^\mathsf{T} &= \begin{bmatrix}\infty & \bar{r}\tan(\lambda_{\text{long}}) & \infty\end{bmatrix},
\end{aligned}$$

are relaxed. The control input sequence is $\mathbf{u}(t+j) = \mathbf{u}^*_{j|t}$, $j = 0, \ldots, N_{\text{fb}} - 1$, where $\mathcal{U}_t^*$ is the minimizer of (17), and N_{fb} is the number of time steps between control updates.

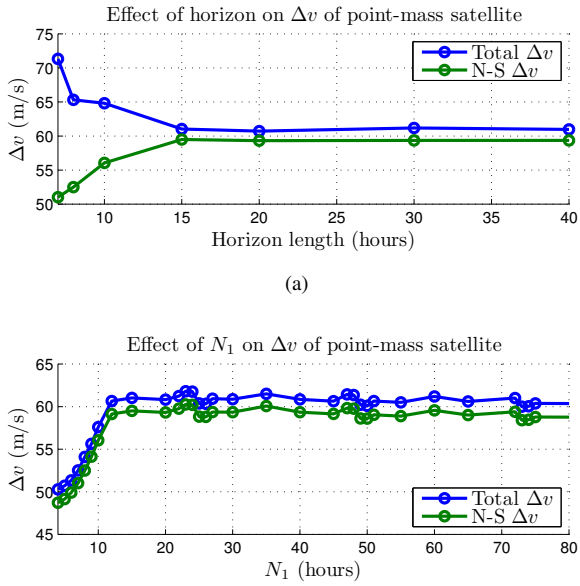

Fig. 5. Plots of annual Δv with a point-mass satellite and a $\pm 0.01^\circ$ station keeping window for varying (a) $N_1 = N_2$ and (b) N_1 with $N_2 = 15$ hours.

The development of a split-horizon MPC policy is motivated by a study on the effect of the prediction horizon on the yearly Δv required to keep a point-mass satellite equipped with 12 electric thrusters and orbital dynamics described by (1) within a $\pm 0.01^\circ$ station keeping window. A plot of the yearly Δv for a non-split prediction horizon ($N_1 = N_2$) ranging from 5 hours to 40 hours is shown in Fig. 5(a), where $\Delta t = 1$ hour. The total Δv clearly increases with decreasing horizon, however, it is observed that the North-South (N-S) component of Δv *decreases* with decreasing horizon. This decrease in N-S Δv is masked in the total Δv by a larger increase in East-West (E-W) Δv with decreasing horizon. The split-horizon MPC policy was developed to address this counterintuitive behavior to retain the best performance in each component of the station keeping problem. The plot of Fig. 5(b) is very similar to the plot of Fig. 5(a), but only the prediction horizon N_1 is varied while $N_2 = 15$ hours is held constant. This plot shows that both the total Δv and the N-S Δv decrease with decreasing N_1 under 12 hours. The total Δv and the N-S Δv also decrease with increasing N_1 over 12 hours, however such decrease is minimal unless N_1 is larger than several days. Indeed, the optimal Δv performance could be achieved by performing predictions using the full nonlinear

model over an infinite horizon, but the resulting policy would be too computationally demanding, especially for on-board implementation. On the other hand, we can achieve suitable performance with a short prediction horizon over the linear dynamics (13) while remaining computationally feasible.

It is postulated that the decrease in Δv observed for shorter N_1 is due to the choice of coordinates used to represent the satellite's orbital dynamics, which only provide for an approximation of the orbital inclination. When the prediction model has some inaccuracies, a longer prediction horizon, which relies more on such model, may delay the control action until the satellite approaches the edges of the station keeping window, away from the orbital nodes, where propulsion is less efficient. Instead, a shorter prediction horizon relies less on the prediction model, yielding a more aggressive control action when the satellite crosses the orbital nodes, which is also more fuel efficient.

Using orbital elements for prediction would allow for directly representing the orbit's inclination, at the price of solving nonlinear optimization problems, and hence increasing, possibly excessively, the computational burden. Investigating a choice of coordinates such that the inclination can be directly represented without increasing excessively the computational burden may be the subject of future research.

E. Thruster Quantization

The low-thrust electric thrusters considered for this spacecraft are operated with on-off pulses. The control input generated by the MPC policy described in Section III-D is a continuous thrust value for each thruster, which cannot be used directly with on-off thrusters, or in the propulsion system assembly shown in Fig. 2, the latter due to not enforcing the constraint on the joint angles γ_n, γ_s on the different booms. As such, the control input must be quantized to on-off pulses that satisfy the physical constraints of the thrusters and the propulsion system assembly. In our initial investigation [34] we developed a PWM quantization scheme with a fixed frequency of five on-off pulses per time step with varying pulse widths, such that the average thrust matched the constant thrust of the MPC control input over each time step. The PWM scheme works well, but leads to a large number of on-off pulses, on the order of 30 pulses per thruster per orbit. Such number of pulses results in more than $160,000$ pulses within a 15 year lifetime of the satellite, which may be too much for many existing electric propulsion thrusters [37]. Thus, to reduce the number of on-off pulses, a single pulse quantization scheme over a feedback period is proposed in this section.

As shown in Fig. 6, consider the quantization of a piecewise constant control input sequence, $\mathbf{u}_{\text{mpc}}$, over a time step beginning at time t_0 and ending at time $t_f = t_0 + N_{\text{fb}}\Delta t$, where $N_{\text{fb}} \in \mathbb{Z}^+$ is the number of discretization time steps in a feedback period, and only a single pulse of magnitude $f_{\max}$ is applied at the i^{th} thruster starting at time $t_{1,i}$ and ending at time $t_{2,i}$, and $t_0 \leq t_{1,i} < t_{2,i} \leq t_f$. The thruster on and off times are solved to minimize the predicted state error due to quantization at the end of the feedback period.

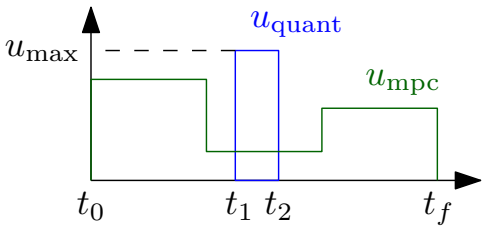

Fig. 6. Single quantized on-off thrust pulse (u_{quant}) over one feedback period with three discrete time steps ($N_{\text{fb}} = 3$) for a given thruster.

The predicted states of the system at time t_f based on the quantized thrust inputs are given by

$$\mathbf{x}_{\text{quant}}(t_f) = e^{\mathbf{A}N_{\text{fb}}\Delta t}\mathbf{x}(t_0) + \sum_{i=1}^{4} e^{\mathbf{A}(t_f - t_{2,i})}\mathbf{B}_{d,i}(t_{1,i}, t_{2,i})\mathbf{u}_{\max,i}, \tag{18}$$

where

$$\mathbf{u}_{\max,i} = \begin{cases} f_{\max}\frac{\bar{\mathbf{u}}_{\text{mpc},t_0,i}}{\|\bar{\mathbf{u}}_{\text{mpc},j|t_0,i}\|} & \|\bar{\mathbf{u}}_{\text{mpc},t_0,i}\| \geq N_{\text{fb}}\epsilon \\ \mathbf{0} & \|\bar{\mathbf{u}}_{\text{mpc},t_0,i}\| < N_{\text{fb}}\epsilon \end{cases},$$

$$\bar{\mathbf{u}}_{\text{mpc},t_0,i} = \sum_{j=0}^{N_{\text{fb}}-1} \mathbf{u}_{\text{mpc},j|t_0,i},$$

$$\mathbf{u}_{\text{mpc},j|t_0}^{\mathsf{T}} = \begin{bmatrix} \mathbf{u}_{\text{mpc},j|t_0,1}^{\mathsf{T}} & \mathbf{u}_{\text{mpc},j|t_0,2}^{\mathsf{T}} & \mathbf{u}_{\text{mpc},j|t_0,3}^{\mathsf{T}} & \mathbf{u}_{\text{mpc},j|t_0,4}^{\mathsf{T}} \end{bmatrix},$$

and $\epsilon > 0$ is the tolerance below which the MPC input is considered to be zero. The calculation of $\mathbf{u}_{\max,i}$ involves averaging the MPC inputs of the i^{th} thruster over the feedback period, which gives a single gimbal angle for each thruster within the feedback period.

The predicted states of the system evolution based on the MPC inputs can be expressed as

$$\begin{aligned} \mathbf{x}_{\text{mpc}}(t_f) &= e^{\mathbf{A}N_{\text{fb}}\Delta t}\mathbf{x}(t_0) + \int_{t_0}^{t_f} e^{\mathbf{A}(t_f-\tau)}\mathbf{B}\mathbf{u}_{\text{mpc}}(\tau)\mathrm{d}\tau \\ &= e^{\mathbf{A}N_{\text{fb}}\Delta t}\mathbf{x}(t_0) + \mathbf{C}_{N_{\text{fb}}-1}\mathbf{u}_{\text{mpc},0:N_{\text{fb}}-1|t_0}, \end{aligned} \tag{19}$$

where $\mathbf{C}_{N_{\text{fb}}-1} = \begin{bmatrix} \mathbf{A}_{\text{d}}^{N_{\text{fb}}-1}\mathbf{B}_{\text{d}} & \cdots & \mathbf{A}_{\text{d}}\mathbf{B}_{\text{d}} & \mathbf{B}_{\text{d}} \end{bmatrix}$ is the controllability matrix, $\mathbf{A}_{\text{d}} = e^{\mathbf{A}\Delta t}$ is the discrete-time $\mathbf{A}$ matrix calculated with time step Δt, $\mathbf{B}_{\text{d}} = \int_0^{\Delta t} e^{\mathbf{A}(\Delta t-\tau)}\mathrm{d}\tau\mathbf{B}$ is the discrete-time $\mathbf{B}$ matrix calculated with time step Δt, and $\mathbf{u}_{\text{mpc},0:N_{\text{fb}}-1|t_0}^{\mathsf{T}} = \begin{bmatrix} \mathbf{u}_{\text{mpc},0|t_0}^{\mathsf{T}} & \cdots & \mathbf{u}_{\text{mpc},N_{\text{fb}}-2|t_0}^{\mathsf{T}} & \mathbf{u}_{\text{mpc},N_{\text{fb}}-1|t_0}^{\mathsf{T}} \end{bmatrix}$. The error between the two predicted states at t_f is given by

$$\begin{aligned} \mathbf{e} &= \mathbf{x}_{\text{mpc}}(t_f) - \mathbf{x}_{\text{quant}}(t_f) \\ &= \mathbf{C}_{N_{\text{fb}}-1}\mathbf{u}_{\text{mpc},0:N_{\text{fb}}-1|t_0} \\ &\quad - \sum_{i=1}^{4} e^{\mathbf{A}(t_f-t_{2,i})}\mathbf{B}_{d,i}(t_{1,i}, t_{2,i})\mathbf{u}_{\max,i}. \end{aligned} \tag{20}$$

The switching times for each thruster must satisfy $t_0 \leq t_{1,i} < t_{2,i} \leq t_f$, $i = 1, 2, 3, 4$. Additionally, there is a requirement that not more than one thruster on the North or South-facing boom-thruster assembly should fire at any given time, which is further motivated by the fact that these thrusters share the

gimbal angle γ_a, $a \in \{n, s\}$, and hence their directions cannot be independently controlled. This results in a constraint on the switching times of the thrusters to enforce that they never overlap. As the firing order of the thrusters may have an impact on the predicted state error, different orders of thruster firings are considered: 1 before 2 and 3 before 4 (Mode 1), as well as 2 before 1 and 4 before 3 (Mode 2). Defining the design variable

$$\mathbf{t}^\mathsf{T} = \begin{bmatrix} t_{1,1} & t_{2,1} & t_{1,2} & t_{2,2} & t_{1,3} & t_{2,3} & t_{1,4} & t_{2,4} \end{bmatrix},$$

the thruster switching constraints can be written as $\mathbf{A}_{t,i}\mathbf{t} \leq \mathbf{b}_{t,i}$, $i = 1, 2$, where $\mathbf{b}_{t,i}^\mathsf{T} = \begin{bmatrix} 0 & 0 & 0 & 0 & -t_0 & t_f & -t_0 & t_f & 0 & 0 \end{bmatrix}$,

$$\mathbf{A}_{t,i} = \begin{bmatrix} \mathbf{A}_t \\ \bar{\mathbf{A}}_{t,i} \end{bmatrix}, \; \mathbf{A}_t = \begin{bmatrix} 1 & -1 & 0 & 0 & 0 & 0 & 0 & 0 \\ 0 & 0 & 1 & -1 & 0 & 0 & 0 & 0 \\ 0 & 0 & 0 & 0 & 1 & -1 & 0 & 0 \\ 0 & 0 & 0 & 0 & 0 & 0 & 1 & -1 \end{bmatrix},$$

and the contents of $\bar{\mathbf{A}}_{t,i}$ depend on the thruster-firing mode considered. The matrix $\mathbf{A}_t$ and the first four rows of $\mathbf{b}_{t,i}$ ensure that $t_{1,i} \leq t_{2,i}$, while $\bar{\mathbf{A}}_{t,i}$ and the last six rows of $\mathbf{b}_{t,i}$ determine the thruster firing order. The contents of $\bar{\mathbf{A}}_{t,i}$ for Modes 1 and 2, respectively, are

$$\bar{\mathbf{A}}_{t,1} = \begin{bmatrix} -1 & 0 & 0 & 0 & 0 & 0 & 0 & 0 \\ 0 & 0 & 0 & 1 & 0 & 0 & 0 & 0 \\ 0 & 0 & 0 & 0 & -1 & 0 & 0 & 0 \\ 0 & 0 & 0 & 0 & 0 & 0 & 0 & 1 \\ 0 & 1 & -1 & 0 & 0 & 0 & 0 & 0 \\ 0 & 0 & 0 & 0 & 0 & 1 & -1 & 0 \end{bmatrix},$$

$$\bar{\mathbf{A}}_{t,2} = \begin{bmatrix} 0 & 0 & -1 & 0 & 0 & 0 & 0 & 0 \\ 0 & 1 & 0 & 0 & 0 & 0 & 0 & 0 \\ 0 & 0 & 0 & 0 & 0 & 0 & -1 & 0 \\ 0 & 0 & 0 & 0 & 0 & 1 & 0 & 0 \\ -1 & 0 & 0 & 1 & 0 & 0 & 0 & 0 \\ 0 & 0 & 0 & 0 & -1 & 0 & 0 & 1 \end{bmatrix}.$$

If no thrusters are on during the feedback period, then all thrust commands are set to zero for the entire period and no optimization problem is solved. Otherwise, the following optimization problem is solved.

$$\min_{t_{1,i},\, t_{2,i},\, i=1,2,3,4} \; \mathbf{e}^\mathsf{T}\mathbf{W}\mathbf{e}, \quad \text{subject to} \quad \mathbf{A}_{t,1}\mathbf{t} \leq \mathbf{b}_{t,1}, \tag{21}$$

where $\mathbf{W} = \mathbf{W}^\mathsf{T} \geq 0$ is a weighting matrix. The same optimization problem is then solved with the constraint $\mathbf{A}_{t,2}\mathbf{t} \leq \mathbf{b}_{t,2}$ instead of $\mathbf{A}_{t,1}\mathbf{t} \leq \mathbf{b}_{t,1}$. The solution that results in a smaller cost function value is used as the optimal solution to the quantization scheme.

The selection of $\mathbf{W}$ greatly influences the quantization results, as it determines which predicted state errors to focus on minimizing. In practice, it is observed that a suitable value of $\mathbf{W}$ is one that scales the magnitudes of the states to be roughly the same, thus providing equal importance to the error in the different states.

IV. Simulation Results

In this section, the MPC policy formulated in Section III is implemented in simulation. A spacecraft orbiting the Earth in a geostationary orbit is considered, with a mass of 4000 kg, and reactions wheels each with a mass of 20 kg, a radius of 0.75 m, and a thickness of 0.2 m. The nominal gimbal angles of the boom-thruster assemblies are $\bar{\alpha}_n = \bar{\alpha}_s = \bar{\beta}_n = \bar{\beta}_s = 0^\circ$ and $\bar{\gamma}_n = \bar{\gamma}_s = 40.14^\circ$. Further details of the physical parameters relating to the boom-thruster assemblies can be found in [34].

The performance constraints considered in simulation include a maximum thruster magnitude of 0.1 N, a station keeping window of $\pm 0.05^\circ$ in both latitude and longitude, and a maximum allowable attitude error of $\pm 0.02^\circ$ in yaw, pitch, and roll. Simulations are performed for 425 orbits beginning at an epoch of Jan. 1, 2000, but only results from the last 365 orbits are presented and used for analysis, in an effort to remove any transient behavior.

The MPC policy uses a split prediction horizon with $N_1 = 5$ hours, $N_2 = 20$ hours, a discretization time step of $\Delta t = 1$ hour, a feedback period of $N_{\text{fb}} = 1$ time step, and weighting matrices of $\mathbf{Q} = \text{diag}\{\mathbf{Q}_\mathbf{r}, \mathbf{Q}_{\dot{\mathbf{r}}}, \mathbf{Q}_{\boldsymbol{\theta}}, \mathbf{Q}_{\boldsymbol{\omega}}, \mathbf{Q}_{\boldsymbol{\nu}}, \mathbf{Q}_{\tilde{\mathbf{x}}_{\text{dist}}}\}$ and $\mathbf{R} = \mathbf{R}_{\text{thrust}} + \mathbf{R}_{\text{torque}}$, where $\mathbf{Q}_\mathbf{r} = 10^{-9} \cdot \text{diag}\{0, 1, 1\}$ 1/m^2, $\mathbf{Q}_{\dot{\mathbf{r}}} = \mathbf{0}$ s^2/m^2, $\mathbf{Q}_{\boldsymbol{\theta}} = 10^{-3} \cdot \mathbf{1}$ 1/rad^2, $\mathbf{Q}_{\boldsymbol{\omega}} = 10^{-3} \cdot \mathbf{1}$ s^2/rad^2, $\mathbf{Q}_{\boldsymbol{\nu}} = 10^{-2} \cdot \mathbf{1}$ s^2/rad^2, $\mathbf{Q}_{\tilde{\mathbf{x}}_{\text{dist}}} = \mathbf{0}$, $\mathbf{R}_{\text{thrust}} = 10^{10}$ 1/N^2, $\mathbf{R}_{\text{torque}} = 10^{10} \cdot \mathbf{L}^\mathsf{T}\mathbf{L}$, where $\mathbf{L} = \text{diag}\{\mathbf{B}_1^\tau, \mathbf{B}_2^\tau, \mathbf{B}_3^\tau, \mathbf{B}_4^\tau\}$. The inner-loop attitude controller gains are $\mathbf{K}_1 = 1 \cdot \mathbf{1}$ 1/s, $\mathbf{K}_p = 20 \cdot \mathbf{1}$ N·m, $\mathbf{K}_\nu = 500 \cdot \mathbf{1}$ N·m·s. The observer dynamics of the inner-loop attitude controller are chosen as $\mathbf{A}_{\text{dist}} = \text{diag}\{\bar{\mathbf{A}}_{\text{dist}}, \bar{\mathbf{A}}_{\text{dist}}, \bar{\mathbf{A}}_{\text{dist}}\}$ and $\mathbf{C}_{\text{dist}} = \text{diag}\{\bar{\mathbf{C}}_{\text{dist}}, \bar{\mathbf{C}}_{\text{dist}}, \bar{\mathbf{C}}_{\text{dist}}\}$, where

$$\bar{\mathbf{A}}_{\text{dist}} = \begin{bmatrix} -0.001 & -\omega_d^2 \\ 1 & -0.001 \end{bmatrix},$$

$\omega_d = 2\pi$ rad/day, and $\bar{\mathbf{C}}_{\text{dist}} = \begin{bmatrix} 1 & 0 \end{bmatrix}$. The observer matrix $\bar{\mathbf{B}}_{\text{dist}}$ is given by $\bar{\mathbf{B}}_{\text{dist}} = \mathbf{P}_{\text{dist}}^{-1}\bar{\mathbf{C}}_{\text{dist}}^\mathsf{T}$, where $\mathbf{P}_{\text{dist}} = \mathbf{P}_{\text{dist}}^\mathsf{T} \geq 0$ satisfies the Lyapunov equation $\bar{\mathbf{A}}_{\text{dist}}^\mathsf{T}\mathbf{P}_{\text{dist}} + \mathbf{P}_{\text{dist}}\bar{\mathbf{A}}_{\text{dist}} = -\mathbf{Q}_{\text{dist}}$ with $\mathbf{Q}_{\text{dist}} = 10^{-3} \cdot \mathbf{1}$.

Simulation of the orbital dynamics is preformed using Systems Tool Kit (STK)/Astrogator, a high-fidelity orbit propagator developed by Analytical Graphics, Inc., while the attitude dynamics are simulated using the nonlinear model in (1b), (1c), and (1d) in continuous time using a high precision ODE integrator[2]. A block diagram of the simulation setup in closed loop with the MPC policy is provided in Fig. 4.

A simulation is first performed with a non-quantized version of the proposed MPC policy (i.e., the quantization of Section III-E is omitted), which yields a Δv of 64.9 m/s. Because there is no constraint on the thrusters firing simultaneously, there are instances in simulation where different gimbal angles are used for the two North or South facing thrusters, which is physically unrealizable. This issue is resolved by the quantization scheme proposed in Section III-E.

A second simulation is performed with the quantized MPC policy of Section III with identical control parameters as the previous simulation and the weighting matrix $\mathbf{W} = \text{diag}\{\mathbf{W}_\mathbf{r}, \mathbf{W}_{\dot{\mathbf{r}}}, \mathbf{W}_{\boldsymbol{\theta}}, \mathbf{W}_{\boldsymbol{\omega}}, \mathbf{W}_{\boldsymbol{\nu}}, \mathbf{W}_{\tilde{\mathbf{x}}_{\text{dist}}}\}$, where $\mathbf{W}_\mathbf{r} = 10^{-10} \cdot$

[2]Currently, it is not possible to perform major changes in the attitude control code of STK and the attitude control module cannot be used by the general public due to Export Control limitations. Thus, we simulate the attitude in parallel by a high precisions ODE integrator. Overall, given that the attitude is kept in a tight range around the equilibrium, the continuous time nonlinear ODE is precise enough for its simulation.

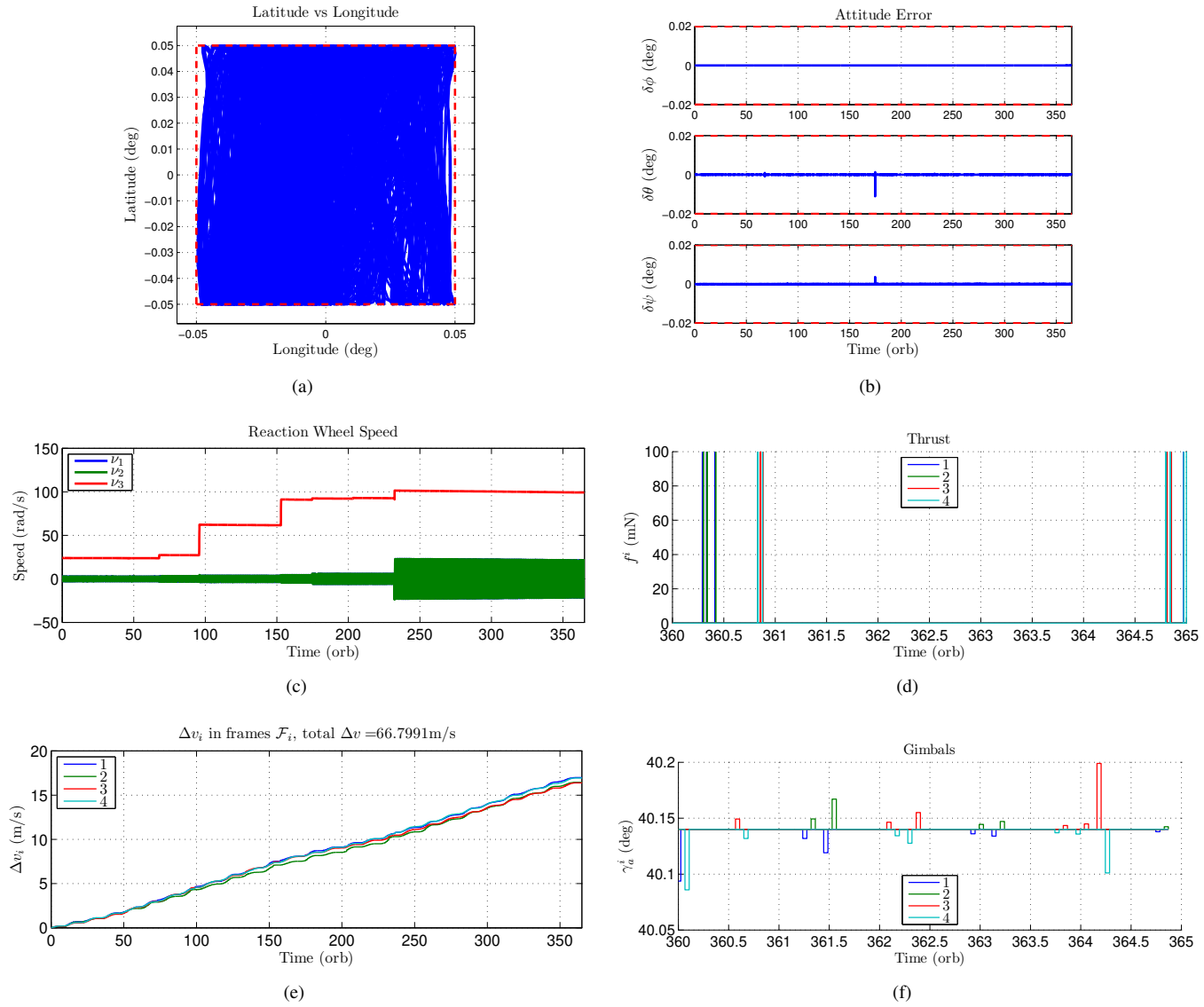

Fig. 7. One year simulation using the quantized MPC policy of Section III with (a) station keeping window, (b) spacecraft attitude error, (c) reaction wheel speeds, (d) thrust forces over the last 5 orbits, (e) accumulation of Δv for each thruster, and (f) gimbal angles over the last 5 orbits.

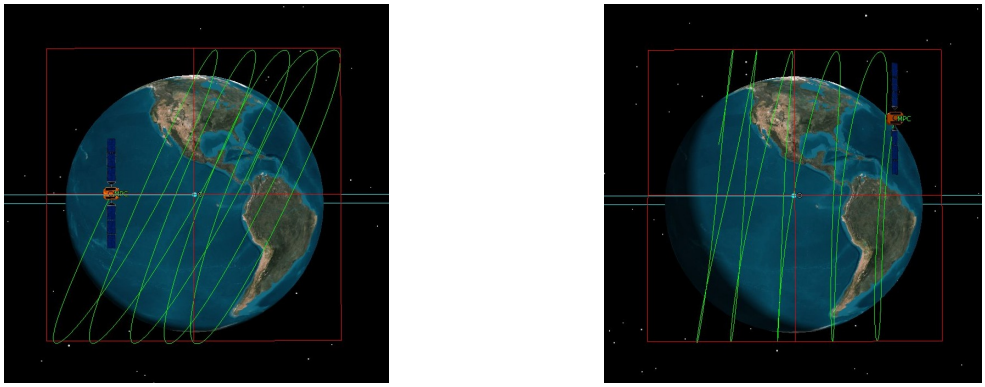

(a) (b)

Fig. 8. Images from the STK simulation taken on (a) May 12, 2000 (orbit 72) and (b) July 30, 2000 (orbit 151). The red square represents the station keeping window, the green trail shows the satellite position over the last 5 orbits, and the size of the satellite is not to scale for illustrative purposes.

$\text{diag}\{1, 1, 10^3\}$ 1/m^2, $\mathbf{W}_{\tilde{\mathbf{r}}} = 10^6 \cdot \mathbf{1}$ s^2/m^2, $\mathbf{W}_{\boldsymbol{\theta}} = 10^4 \cdot \mathbf{1}$ 1/rad^2, $\mathbf{W}_{\boldsymbol{\omega}} = 10^{-1} \cdot \mathbf{1}$ s^2/rad^2, $\mathbf{W}_{\boldsymbol{\nu}} = 10 \cdot \mathbf{1}$ s^2/rad^2, and $\mathbf{W}_{\tilde{\mathbf{x}}_{\text{dist}}} = 10 \cdot \mathbf{1}$. The results of this simulation are included in Fig. 7, where a Δv of 66.8 m/s is achieved with an average of 2.98 pulses per thruster per orbit. Figs. 7(a), 7(b), 7(c) show that constraints are satisfied throughout the simulation. The quantized nature of the thrust inputs is observed in Fig. 7(d). Images from the STK simulation taken at two difference times are provided in Fig. 8 to illustrate how the satellite moves within the station keeping window.

As mentioned earlier, the idealized Δv for NSSK depends on the epoch and station keeping window size, requiring approximately 41–51 m/s/year [5]. Allowing an additional 5% Δv for "East-West" Station-Keeping (EWSK) and momentum management and translating the idealized range to account for the nominal cant angle of the thruster boom assemblies by dividing it by $\cos(40.14^\circ)$, we arrive at an expected total Δv consumption of 56–70 m/s/year. We find our result of 66.8 m/s (and 2.98 pulses per thruster per orbit) to be squarely within that range, indicating that we are as close to the ideal as possible despite adding additional limitations due to quantization. The fuel consumption with the quantized MPC policy is significantly lower than the previous result for the same satellite configuration in [34], which required an annual Δv of 79.8 m/s (and ∼30 pulses per thruster per orbit). This savings is predominantly due to the novel split-horizon MPC policy. Table I summarizes and compares the Δv values and features of the results obtained in this work to that of the idealized case and our prior work, highlighting whether the Δv result accounts for EWSK, the thruster geometry of Sec. II, and quantized thrust values.

TABLE I
Δv SUMMARY FOR THE MPC POLICIES IN THIS WORK COMPARED TO THOSE OF THE IDEALIZED CASE AND PRIOR WORK

	EWSK	Sec. II Geometry	On-Off	Δv (m/s)
Ideal [5]	N	N	N	41–51
Ref. [20]	N	N	N	59
Policy III-D applied to [20]	N	N	N	46
Ideal [5] accounting for Sec. II geometry	Y	Y	N	56–70
Policy III-D	Y	Y	N	64.9
Ref. [34]	Y	Y	Y	79.8
Policy III-E	Y	Y	Y	66.8

It is worth noting in Fig. 7(c) that the reaction wheel speed ν_3 deviates from the equilibrium point $\nu_3 = 0$ rad/s used in the linearization of the MPC prediction model in (11), eventually reaching a steady-state value of 100 rad/s. The MPC prediction model could be improved by periodically updating the linearization about a new equilibrium point with a non-zero value of ν_3, i.e., updating $\mathbf{A}_{\text{d}}$ in the prediction model at each time step. For reducing computational burden and code complecity, the MPC prediction model used in this paper relies on a linearization about $\nu_3 = 0$ rad/s and does not recompute the matrix $\mathbf{A}_{\text{d}}$ as ν_3 deviates from 0 rad/s.

V. Quantization Scheme and Robustness Assessment

This section presents in-depth numerical analyses of the parameters used in the single-pulse quantization scheme of Section III-E and the robustness of the proposed MPC policy to realistic model uncertainties and measurement noise. Due to the large number of data points tested, numerical simulations are not performed with STK, but instead with the nonlinear spacecraft dynamic model presented in (1), which was been validated using STK in [20]. Acceleration perturbations due to Earth's oblateness, solar and lunar gravitational attraction, and solar radiation pressure are included in the simulation based on the numerical values in [43]. Solar radiation pressure is also considered in the calculation of a disturbance torque, and is calculated as done in [44, p. 229], with a mean surface area of 200 m^2, surface reflectance of 0.6, solar facing area of $S_{\text{facing}} = 37.5$ m^2, and a solar radiation constant of $C_{\text{srp}} = 4.5 \times 10^{-6}$ N/m^2. The results presented in this section are given as a percent increase or decrease in performance of Δv or pulses/thruster/orbit.

A. Analysis of Quantization Scheme

The selection of the parameters used in the single-pulse quantization scheme of Section III-E is discussed and analyzed numerically in simulation. The quantization parameters considered in this analysis include the thrust cutoff value (ϵ), the number of time steps between feedback (N_{fb}), the weighting matrix used in the quantization objective function ($\mathbf{W}$), and adding an additional constraint preventing the overlapping of any thruster pulses.

1) Thrust Cutoff Value (ϵ): The thrust cutoff value, ϵ, determines the smallest thrust magnitude to quantize as an on-off thruster pulse, whereas every thrust smaller than ϵ is simply ignored. A lower bound on ϵ may be determined by the specifications of the thruster, as on-off electric thrusters often have a minimum pulse width. However, using the lowest possible value of ϵ may not yield the best Δv performance and/or a reasonable number of thruster pulses. Simulations are performed with cutoff values in the range 0.001 mN $\leq \epsilon \leq$ 1 mN to quantify the effect of varying ϵ on performance, and the results are presented in Fig. 9. Fig. 9 shows that the relationships between ϵ and the performance indices Δv and the number of on-off pulses per thruster per orbit is non-trivial. A small value of ϵ can yield reasonable Δv, but results in many thruster pulses (e.g., a 5.6% increase in Δv and 452% increase in the number of pulses/thruster/orbit with $\epsilon = 0.001$ mN compared to the baseline of $\epsilon = 0.01$ mN). A small value of ϵ also helps reduce the effect of quantization on momentum management. For example, Fig. 10 shows that with $\epsilon = 0.001$ mN the reaction wheel speeds are much more similar to the reaction wheel speeds without quantization than with $\epsilon = 0.01$ mN, and momentum management is

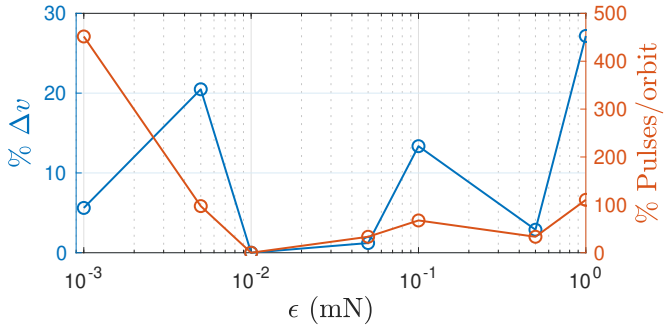

Fig. 9. Effect of varying ϵ in quantization scheme.

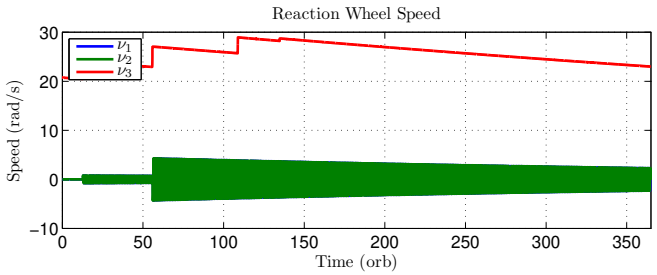

(a)

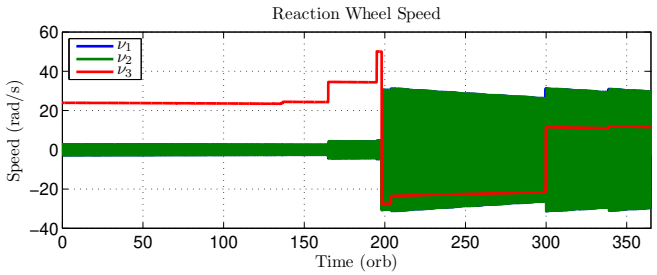

(b)

Fig. 10. STK simulation results: reaction wheel speeds with (a) non-quantized split-horizon MPC policy and (b) quantized split-horizon MPC policy with $\epsilon = 0.001$ mN.

clearly occurring. A large value of ϵ will typically result in a relatively lower number of thruster pulses, but a large Δv (e.g., a 27.2% increase in Δv and 110% increase in the number of pulses/thruster/orbit with $\epsilon = 1$ mN compared to the baseline of $\epsilon = 0.01$ mN). The choice of ϵ ultimately depends on the problem at hand, and is shown to be an important tuning parameter in obtaining optimal performance. In our simulations, the optimum is achieved by an intermediate value ($\epsilon = 0.01$ mN).

2) Number of Time Steps Between Feedback (N_{fb}): A feature of the proposed quantization scheme is that a single pulse can be generated for a feedback period that spans more than one discrete time step. The number of time steps between feedback periods is determined by the positive integer parameter N_{fb}. It is observed in simulation that there is an upper bound on N_{fb} determined by the controller parameters, beyond which the error induced by quantization becomes too large to satisfy state constraints. For the controller parameters used in Section IV with a split horizon of $N_1 = 5$ hours and $N_2 = 20$ hours, only $N_{\text{fb}} = 1$ is feasible. Therefore, to

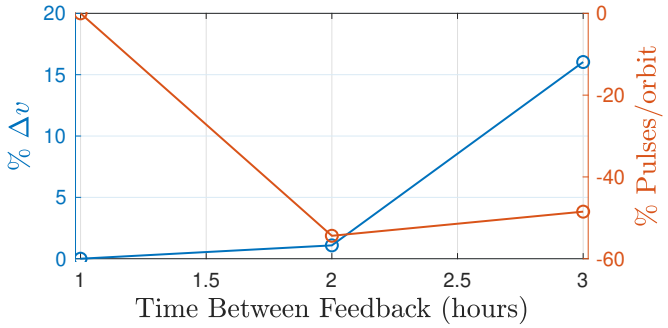

Fig. 11. Effect of varying N_{fb} in quantization scheme.

TABLE II
EFFECT OF VARYING $\mathbf{W}$ IN QUANTIZATION SCHEME

	% Δv	% Pulses
$\mathbf{W}_2$	14.6	97.4
$\mathbf{W}_3$	1.5	36.7

illustrate the effect of N_{fb} on performance, simulations are performed with a non-split horizon of $N_1 = N_2 = 20$ hours with $N_{\text{fb}} = 1$, $N_{\text{fb}} = 2$, and $N_{\text{fb}} = 3$. The results in Fig. 11 demonstrate how using $N_{\text{fb}} = 2$ reduces the number of pulses by 54.4%, but increases Δv by 1.1% compared to $N_{\text{fb}} = 1$. The selection of $N_{\text{fb}} = 3$ yields a more significant increase of 16.0% in Δv and a less significant decrease of 48.5% in the number of thruster pulses compared to $N_{\text{fb}} = 1$. As demonstrated, tuning N_{fb} typically allows for a tradeoff in Δv and the number of thruster pulses, but this tuning may be restricted depending on the problem at hand.

3) Weighting Matrix ($\mathbf{W}$): The selection of the weighting matrix used to formulate the objective function in the quantization scheme has a significant influence on the quantization results, as the value of $\mathbf{W}$ dictates which state errors to focus on minimizing during quantization. Three different choices of $\mathbf{W}$ are examined in this section: $\mathbf{W}_1$ is the same as $\mathbf{W}$ used in Section IV, $\mathbf{W}_2 = \mathbf{W}_1^{1/2}$, and $\mathbf{W}_3 = \mathbf{1}$. Results of $\mathbf{W}_2$ and $\mathbf{W}_3$ relative to $\mathbf{W}_1$ are given in Table II, where both $\mathbf{W}_2$ and $\mathbf{W}_3$ increase Δv and the number of thruster pulses. Based on the authors' experience, it is beneficial to use a weighting matrix that normalize all of the states to roughly the same order of magnitude, which is how $\mathbf{W}_1$ was chosen.

4) Overlapping of Pulses: In some circumstances, most likely due to power limitations [17], it may be required that no thrusters fire simultaneously. An additional constraint can be placed on the thruster pulse times to ensure that no thruster pulses overlap. In this case, three thruster-firing-order modes are considered: $1-2-3-4$ (Mode 1), $2-1-4-3$ (Mode 2), and $3-4-1-2$ (Mode 3). More modes would be required if all possible permutations of the firing order were considered, but typically only two thrusters fire within a given time step (excluding the combinations 1-3 and 2-4), so this is unnecessary. The constraints are written as $\mathbf{A}_{t,i}\mathbf{t} \leq \mathbf{b}_{t,i}$, $i = 1, 2, 3$, where $\mathbf{b}_{t,i}^{\mathsf{T}} = \begin{bmatrix} 0 & 0 & 0 & 0 & -t_0 & t_f & 0 & 0 & 0 \end{bmatrix}$, $\mathbf{A}_{t,i}^{\mathsf{T}} = \begin{bmatrix} \mathbf{A}_t^{\mathsf{T}} & \bar{\mathbf{A}}_{t,i}^{\mathsf{T}} \end{bmatrix}$, $\mathbf{A}_t$ is defined in Section III-E, and the

TABLE III
MEASUREMENT NOISE ROBUSTNESS ASSESSMENT RESULTS

Meas.	Sensor	Bias	Standard Deviation	$\%\,\Delta v$	$\%$ Pulses
Baseline	–	–	–	0	0
$\tilde{\mathbf{r}}_g^{cw}$	GPS	$b_{\mathbf{r}_i} = 0$ m	$\sigma_{\mathbf{r}_i} = 10$ m	22.6	77.9
$\tilde{\mathbf{r}}_g^{cw}$	GPS with KF	$b_{\mathbf{r}_i} = 0$ m	$\sigma_{\mathbf{r}_i} = 10$ m	1.81	24
$\tilde{\mathbf{r}}_g^{cw}$	TLE	$b_{\mathbf{r}_i} = 50$ m	$\sigma_{\mathbf{r}_i} = 500$ m	71	66.3
$\dot{\tilde{\mathbf{r}}}_g^{cw}$	GPS with KF	$b_{\dot{\mathbf{r}}_i} = 0$ m/s	$\sigma_{\dot{\mathbf{r}}_i} = 0.1$ m/s	1.8	4.9
$\tilde{\mathbf{r}}_g^{cw}$ and $\dot{\tilde{\mathbf{r}}}_g^{cw}$	GPS with KF	$b_{\mathbf{r}_i} = 0$ m, $b_{\dot{\mathbf{r}}_i} = 0$ m/s	$\sigma_{\mathbf{r}_i} = 10$ m, $\sigma_{\dot{\mathbf{r}}_i} = 0.1$ m/s	21.9	94.8
$\delta\tilde{\boldsymbol{\theta}}$	Star Tracker	$b_\theta = 3 \times 10^{-5}$ deg	$\sigma_\theta = 3 \times 10^{-3}$ deg	2	4.5
$\tilde{\boldsymbol{\omega}}_p^{pg}$	High-Acc. Gyro	$b_{\omega_i} = 1 \times 10^{-9}$ rad/s	$\sigma_{\omega_i} = 1 \times 10^{-10}$ rad/s	12.1	26.6
$\tilde{\boldsymbol{\omega}}_p^{pg}$	Low-Acc. Gyro	$b_{\omega_i} = 5 \times 10^{-3}$ rad/s	$\sigma_{\omega_i} = 2 \times 10^{-7}$ rad/s	25.5	124.3
$\tilde{\boldsymbol{\nu}}$	Tachometer	$b_{\nu_i} = 0.06$ rad/s	$\sigma_{\nu_i} = 1.6$ rad/s	5.9	40

contents of $\bar{\mathbf{A}}_{t,i}$ depend on the thruster-firing mode considered. The matrix $\mathbf{A}_t$ and the first four rows of $\mathbf{b}_{t,i}$ ensure that $t_{1,i} \leq t_{2,i}$, while $\bar{\mathbf{A}}_{t,i}$ and the last six rows of $\mathbf{b}_{t,i}$ determine the thruster firing order. The contents of $\bar{\mathbf{A}}_{t,i}$ for Modes 1, 2, and 3, respectively, are

$$\bar{\mathbf{A}}_{t,1} = \begin{bmatrix} -1 & 0 & 0 & 0 & 0 & 0 & 0 & 0 \\ 0 & 0 & 0 & 0 & 0 & 0 & 0 & 1 \\ 0 & 1 & -1 & 0 & 0 & 0 & 0 & 0 \\ 0 & 0 & 0 & 1 & -1 & 0 & 0 & 0 \\ 0 & 0 & 0 & 0 & 0 & 1 & -1 & 0 \end{bmatrix},$$

$$\bar{\mathbf{A}}_{t,2} = \begin{bmatrix} 0 & 0 & -1 & 0 & 0 & 0 & 0 & 0 \\ 0 & 0 & 0 & 0 & 0 & 1 & 0 & 0 \\ -1 & 0 & 0 & 1 & 0 & 0 & 0 & 0 \\ 0 & 1 & 0 & 0 & 0 & 0 & -1 & 0 \\ 0 & 0 & 0 & 0 & -1 & 0 & 0 & 1 \end{bmatrix},$$

$$\bar{\mathbf{A}}_{t,3} = \begin{bmatrix} 0 & 0 & 0 & 0 & -1 & 0 & 0 & 0 \\ 0 & 0 & 0 & 1 & 0 & 0 & 0 & 0 \\ 0 & 1 & -1 & 0 & 0 & 0 & 0 & 0 \\ -1 & 0 & 0 & 0 & 0 & 0 & 0 & 1 \\ 0 & 0 & 0 & 0 & 0 & 1 & -1 & 0 \end{bmatrix}.$$

The procedure to solve for the optimal switching times $t_{1,i}$, $t_{2,i}$, $i = 1, 2, 3, 4$, is similar to the procedure outlined in Section III-E, but instead solutions for the three thruster-firing-order modes are found. The solution that yields the lowest cost function value is chosen as the optimal set of switching times.

A simulation is performed using these additional constraints to ensure that no thruster pulses overlap, which increases Δv by 18.5% and increases pulses/thruster/orbit by 105.6%. Enforcing these constraints at all times clearly degrades the performance. However, it is interesting that the proposed control policy can handle this situation, as the power limitation may be due to unforseen circumstances, such as a special fault recovery mode. In such a situation, the quantization constraints in Section III-E can be implemented for most of the orbit and the constraints outlined in this section can be implemented during the intervals in which there is a limitation on power. Thus, the simulation shows that our control strategy is capable of handling situations with limited power, although, with an increase in fuel consumption.

B. Robustness Assessment

In this section, the robustness of the proposed MPC policy is analyzed and tested subject to various forms of measurement noise and uncertainty in the thruster and the spacecraft models.

1) Measurement Noise: In practice, sensors will be used to measure the states of the system either directly or indirectly. Each measurement inherently features some level of noise, which leads to uncertainty in the system states. The purpose of the measurement noise analysis presented here is not necessarily to improve the uncertainty in the states by designing filters or estimators, but to determine whether the levels of measurement noise that can be tolerated by the proposed MPC policy are realistic. The measurement noise considered includes the translational position and velocity of the spacecraft, the attitude and angular velocity of the spacecraft, and the angular rates of the spacecraft's reaction wheels.

The measurement of the spacecraft's position is given by $\tilde{\mathbf{r}}_g^{cw} = \mathbf{r}_g^{cw} + \mathbf{w}_\mathbf{r}$, where $\mathbf{w}_\mathbf{r} \sim \mathcal{N}(\mathbf{b}_\mathbf{r}, \mathbf{V}_\mathbf{r})$, $\mathbf{b}_\mathbf{r}^\mathsf{T} = \begin{bmatrix} b_{\mathbf{r}_x} & b_{\mathbf{r}_y} & b_{\mathbf{r}_z} \end{bmatrix}$, and $\mathbf{V}_\mathbf{r} = \text{diag}\{\sigma_{\mathbf{r}_x}^2, \sigma_{\mathbf{r}_y}^2, \sigma_{\mathbf{r}_z}^2\}$. In this analysis, two levels of uncertainty are considered: 1) GPS-level accuracy [45] ($b_{\mathbf{r}_i} = 0$ m and $\sigma_{\mathbf{r}_i} = 10$ m, $i = x, y, z$), and 2) two-line element (TLE) [46] or ground-based antenna ranging data [47] ($b_{\mathbf{r}_i} = 50$ m and $\sigma_{\mathbf{r}_i} = 500$ m, $i = x, y, z$).

The measurement of the spacecraft's velocity is given by $\dot{\tilde{\mathbf{r}}}_g^{cw} = \dot{\mathbf{r}}_g^{cw} + \mathbf{w}_{\dot{\mathbf{r}}}$, where $\mathbf{w}_{\dot{\mathbf{r}}} \sim \mathcal{N}(\mathbf{b}_{\dot{\mathbf{r}}}, \mathbf{V}_{\dot{\mathbf{r}}})$, $\mathbf{b}_{\dot{\mathbf{r}}}^\mathsf{T} = \begin{bmatrix} b_{\dot{\mathbf{r}}_x} & b_{\dot{\mathbf{r}}_y} & b_{\dot{\mathbf{r}}_z} \end{bmatrix}$, and $\mathbf{V}_{\dot{\mathbf{r}}} = \text{diag}\{\sigma_{\dot{\mathbf{r}}_x}^2, \sigma_{\dot{\mathbf{r}}_y}^2, \sigma_{\dot{\mathbf{r}}_z}^2\}$. For this analysis, GPS-level accuracy is considered, where $b_{\dot{\mathbf{r}}_i} = 0$ cm/s and $\sigma_{\dot{\mathbf{r}}_i} = 10$ cm/s, $i = x, y, z$.

The measurement of the spacecraft's attitude is perturbed by the DCM $\tilde{\mathbf{C}}$, such that $\tilde{\mathbf{C}}_{pg} = \tilde{\mathbf{C}}\mathbf{C}_{pg}$. An axis-angle parameterization is used to define $\tilde{\mathbf{C}} = \cos w_\theta \mathbf{1} + (1 - \cos w_\theta)\,\hat{\mathbf{a}}\hat{\mathbf{a}}^\mathsf{T} + \sin w_\theta \hat{\mathbf{a}}^\times$, where $w_\theta \sim \mathcal{N}(b_\theta, \sigma_\theta^2)$, $\hat{\mathbf{a}} = \mathbf{a}/\left\|\mathbf{a}\right\|_2$, $\mathbf{a} \sim \mathcal{N}(0, \mathbf{1})$. Measurement noise associated with the use of a star tracker is considered, where $b_\theta = 3 \times 10^{-5}$ deg and $\sigma_\theta = 3 \times 10^{-3}$ deg [48–50].

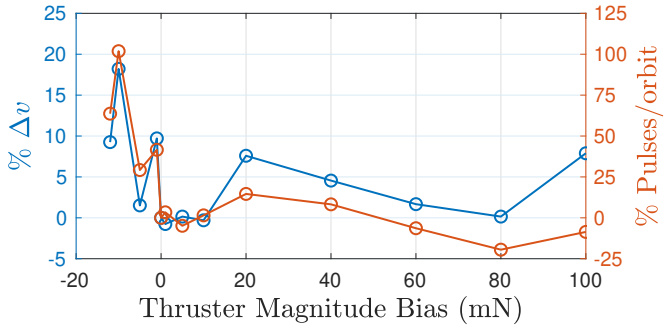

Fig. 12. Thruster magnitude uncertainty robustness assessment results.

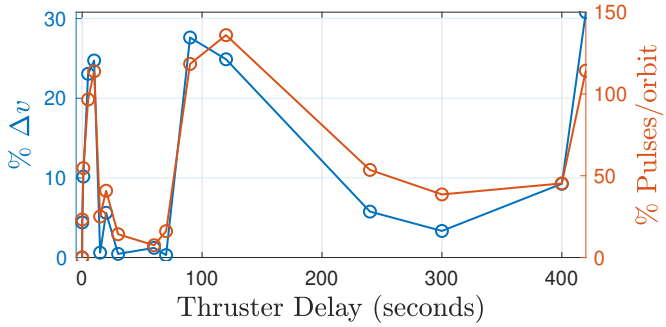

Fig. 13. Thruster delay robustness assessment results.

The measurement of the spacecraft's angular velocity is given by $\tilde{\boldsymbol{\omega}}_p^{pg} = \boldsymbol{\omega}_p^{pg} + \mathbf{w}_{\boldsymbol{\omega}}$, where $\mathbf{w}_{\boldsymbol{\omega}} \sim \mathcal{N}(\mathbf{b}_{\boldsymbol{\omega}}, \mathbf{V}_{\boldsymbol{\omega}})$, $\mathbf{b}_{\boldsymbol{\omega}}^{\mathsf{T}} = \begin{bmatrix} b_{\omega_1} & b_{\omega_2} & b_{\omega_3} \end{bmatrix}$, and $\mathbf{V}_{\boldsymbol{\omega}} = \text{diag}\{\sigma_{\omega_1}^2, \sigma_{\omega_2}^2, \sigma_{\omega_3}^2\}$. Measurement noise associated with a high-accuracy rate gyroscope [51] ($b_{\omega_i} = 1 \times 10^{-9}$ rad/s and $\sigma_{\omega_i} = 1 \times 10^{-10}$ rad/s, $i = 1, 2, 3$) and a low-accuracy rate gyroscope [52] ($b_{\omega_i} = 5 \times 10^{-3}$ rad/s and $\sigma_{\omega_i} = 2 \times 10^{-7}$ rad/s, $i = 1, 2, 3$) are considered.

The measurement of the spacecraft's reaction wheel speeds is given by $\tilde{\boldsymbol{\nu}} = \boldsymbol{\nu} + \mathbf{w}_{\boldsymbol{\nu}}$, where $\mathbf{w}_{\boldsymbol{\nu}} \sim \mathcal{N}(\mathbf{b}_{\boldsymbol{\nu}}, \mathbf{V}_{\boldsymbol{\nu}})$, $\mathbf{b}_{\boldsymbol{\nu}}^{\mathsf{T}} = \begin{bmatrix} b_{\nu_1} & b_{\nu_2} & b_{\nu_3} \end{bmatrix}$, and $\mathbf{V}_{\boldsymbol{\nu}} = \text{diag}\{\sigma_{\nu_1}^2, \sigma_{\nu_2}^2, \sigma_{\nu_3}^2\}$. Realistic measurement noise from a reaction wheel tachometer is considered, where $b_{\nu_i} = 0.06$ rad/s and $\sigma_{\nu_i} = 1.6$ rad/s, $i = 1, 2, 3$ [53].

Results with the various individual measurement noises are presented in Table III, where it is shown that the MPC policy is particularly sensitive to translational position and velocity measurements, but remains robust to realistic measurement noise when a simple Kalman filter is implemented.

2) Thruster Model Uncertainty: The actual thrusters of the spacecraft are not ideal, and will contain some amount of uncertainty. Specifically, uncertainty in the magnitude of the thrust, time delays in the thruster pulse, and thruster misalignment are considered in this section.

Uncertainty in the magnitude of the thrust may be due to a leaking or stuck valve, uncertainty in the thruster controller, etc. Thruster magnitude uncertainty is modeled as $\tilde{f}_{\max} = f_{\max} + b_f$. The results of simulations performed with values $-0.16 f_{\max} \leq b_f \leq f_{\max}$ are presented in Fig. 12, which show that the MPC policy is robust to a significant amount of thruster magnitude uncertainty. The MPC policy is clearly more robust to perturbations that increase the thruster magnitude, which is intuitive, as additional unexpected control authority is available in this case.

TABLE IV
MASS UNCERTAINTY ROBUSTNESS ASSESSMENT RESULTS

w_m (kg)	% Δv	% Pulses
-400	1.4	10.1
$+400$	1.2	17.6

TABLE V
CENTER OF MASS UNCERTAINTY ROBUSTNESS ASSESSMENT RESULTS

$\mathbf{r}_p^{\tilde{c}c^{\mathsf{T}}}$ (cm)	% Δv	% Pulses
[0.5 0 0]	2.6	16.1
[5 0 0]	15	428.5
[0 0.5 0]	0.3	30
[0 5 0]	1.2	19.9
[0 0 0.5]	20.6	91.8
[0 0 5]	25.5	113.1
[−0.5 0 0]	9.4	79.4
[−5 0 0]	8.6	573.8
[0 −0.5 0]	20.3	95.1
[0 −5 0]	SK constraints violated	
[0 0 −0.5]	13.3	76.4
[0 0 −5]	17.8	82.4

Time delays are implemented in simulation as $\tilde{t}_{1,i} = t_{1,i} + \delta t$ and $\tilde{t}_{2,i} = t_{2,i} + \delta t$, $i = 1, 2, 3, 4$, where δt is the time delay, and $\tilde{t}_{1,i}$ and $\tilde{t}_{2,i}$ are the delayed "on time" and "off time" of the thruster pulse, respectively. Results of simulations with time delay values of $0 \leq \delta t \leq 420$ s are presented in Fig. 13, which illustrate that a time delay of 20 seconds can be tolerated with less than a 1% increase in Δv and less than a 16% increase in the number of thruster pulses, while time delays of up to 2 minutes can be tolerated with less than a 10% increase in Δv and around 4 pulses/thruster/orbit.

Misalignment of the thrusters is common on satellites due to the extreme forces and vibrations experienced during launch. $\tilde{\mathbf{C}}_{ia} = \mathbf{C}_1(\delta_i)\mathbf{C}_2(\tilde{\beta}_a)\mathbf{C}_3(\tilde{\alpha}_a)$, where $\tilde{\alpha}_a$ and $\tilde{\beta}_a$ are constant angles that are randomly assigned prior to simulation using $\tilde{\alpha}_a \sim \mathcal{N}(\bar{\alpha}_a, \sigma_\alpha^2)$, $\tilde{\beta}_a \sim \mathcal{N}(\bar{\beta}_a, \sigma_\beta^2)$. Twelve simulations are performed with $\sigma_\alpha = \sigma_\beta = 0.1$ deg, which yields an average Δv increase of 7.9% and an average increase in pulses/thruster/orbit of 74.2%.

3) Model Uncertainty: Another source of uncertainty considered in this robustness assessment is in the spacecraft's mass and center of mass. Simulations are performed with $\tilde{m}_{\mathcal{B}} = m_{\mathcal{B}} + w_m$, where $m_{\mathcal{B}}$ is the nominal spacecraft mass, $\tilde{m}_{\mathcal{B}}$ is the uncertain spacecraft mass, and $-0.1 m_{\mathcal{B}} \leq w_m \leq 0.1 m_{\mathcal{B}}$. The center of mass of the spacecraft is also perturbed as $\mathbf{r}_p^{\tilde{c}c^{\mathsf{T}}} = \begin{bmatrix} r_{p1}^{\tilde{c}c} & r_{p2}^{\tilde{c}c} & r_{p3}^{\tilde{c}c} \end{bmatrix}$, where -5 cm $\leq r_{pi}^{\tilde{c}c} \leq 5$ cm, $i = 1, 2, 3$. Results with these perturbations are presented in

Tables IV and V. The MPC policy is shown to be quite robust to both types of mass uncertainty, particularly to uncertainty in the total mass and the location of the center of mass in the $\underrightarrow{p}^{1}$ direction.

VI. Conclusions

The novel split-horizon MPC policy presented in this paper is shown to be effective in performing simultaneous station keeping and momentum management of a GEO satellite. Quantization of the thruster is performed using a single-pulse quantization method, which reduces the number of pulses compared to PWM methods and results in control inputs that are implementable with existing electric propulsion technology. Robustness assessment studies demonstrated the performance of the control policy with various forms of uncertainty and measurement noise, which further validates the proposed method.

ACKNOWLEDGMENT

The authors would like to thank Dr. Alex Walsh and Dr. David Zlotnik for contributions to initial studies related to this work, while they were interns at Mitsubishi Electric Research Laboratories.

References

[1] D. M. Goebel and I. Katz, *Fundamentals of Electric Propulsion: Ion and Hall Thrusters*. John Wiley & Sons, 2008, vol. 1.

[2] M. Sabbadini, M. Buoso, and G. Saccocia, "Electric propulsion," Tech. Rep., 2002.

[3] K. E. Clark, "Survey of electric propulsion capability," *Jour. Spacecraft and Rockets*, vol. 12, no. 11, pp. 641–654, 1975.

[4] W. A. Hoskins, R. J. Cassady, O. Morgan, R. M. Myers, F. Wilson, D. Q. King, and K. deGrys, "30 years of electric propulsion flight experience at aerojet rocketdyne," in *33rd Int. Electric Propulsion Conf., Washington DC*, 2013.

[5] M. Martinez-Sanchez and J. E. Pollard, "Spacecraft electric propulsion-an overview," *Jour. Propulsion and Power*, vol. 14, no. 5, pp. 688–699, 1998.

[6] H. Kuninaka and K. Kajiwara, "Overview of JAXA's activities on electric propulsion," in *Proc. 32nd Int. Electric Propulsion Conf.*, Wiesbaden, Germany, 2011, p. 332.

[7] E. M. Soop, *Handbook of Geostationary Orbits*. Springer, 1994.

[8] A. Sukhanov and A. Prado, "On one approach to the optimization of low-thrust station keeping manoeuvres," *Adv. Space Research*, vol. 50, no. 11, pp. 1478 – 1488, 2012.

[9] M. Leomanni, A. Garulli, A. Giannitrapani, and F. Scortecci, "All-electric spacecraft precision pointing using model predictive control," *Jour. Guidance, Control, and Dynamics*, vol. 38, no. 1, pp. 161–168, 2015.

[10] C. Gazzino, D. Arzelier, L. Cerri, D. Losa, C. Louembet, and C. Pittet, "Solving the minimum-fuel low-thrust geostationary station keeping problem via the switching systems theory," in *7th European Conf. for Aeronautics and Space Sciences*, Milano, Italy, July 2017.

[11] C. Gazzino, D. Arzelier, D. Losa, C. Louembet, C. Pittet, and L. Cerri, "Optimal control for minimum-fuel geostationary station keeping of satellites equipped with electric propulsion," *IFAC Papers Online*, vol. 49, no. 17, pp. 379–384, 2016.

[12] Y. Ulybyshev, "Long-term station keeping of space station in lunar halo orbits," *Jour. Guidance, Control, and Dynamics*, vol. 38, no. 6, pp. 1063–1070, 2014.

[13] A. Garulli, A. Giannitrapani, M. Leomanni, and F. Scortecci, "Autonomous low-earth-orbit station-keeping with electric propulsion," *Jour. Guidance, Control, and Dynamics*, vol. 34, no. 6, pp. 1683–1693, 2011.

[14] M. Leomanni, E. Rogers, and S. B. Gabriel, "Explicit model predictive control approach for low-thrust spacecraft proximity operations," *Jour. Guidance, Control, and Dynamics*, vol. 37, no. 6, pp. 1780–1790, 2014.

[15] R. Vazquez, F. Galivan, and E. F. Camacho, "Pulse-width predictive control for LTV systems with application for spacecraft rendez-vous," *Control Engineering Practice*, vol. 60, pp. 199–210, March 2017.

[16] C. Gazzino, C. Louembet, D. Arzelier, N. Jozefowiez, D. Losa, C. Pittet, and L. Cerri, "Integer programming for optimal control of geostationary station keeping of low-thrust satellites," LAAS Report 16341, July 2017.

[17] C. Gazzino, D. Arzelier, C. Louembet, L. Cerri, C. Pittet, and D. Losa, "Long-term electric-propulsion geostationary station-keeping via integer programming," *Jour. Guidance, Control, and Dynamics*, vol. 42, no. 5, pp. 976–991, 2019.

[18] C. Gazzino, D. Arzelier, L. Cerri, D. Losa, C. Louembet, and C. Pittet, "A three-step decomposition method for solving the minimum-fuel geostationary station keeping of satellites equipped with electric propulsion," *Acta Astronautica*, vol. 158, pp. 12–22, May 2019.

[19] L. Li, J. Zhang, Y. Li, and S. Zhao, "Geostationary station-keeping with electric propulsion in full and failure modes," *Acta Astronautica*, 2019, to appear.

[20] A. Weiss, U. V. Kalabić, and S. Di Cairano, "Station keeping and momentum management of low-thrust satellites using MPC," *Aerospace Science and Technology*, vol. 76, pp. 229–241, May 2018.

[21] J. Climer. Boeing: World's first all-electric propulsion satellite begins operations. [Online]. Available: https://boeing.mediaroom.com/2015-09-10-Boeing-World-s-First-All-Electric-Propulsion-Satellite-Begins-Operations

[22] D. Losa, M. Lovera, J.-P. Marmorat, T. Dargent, and J. Amalric, "Station keeping of geostationary satellites with on-off electric thrusters," in *Proc. 2006 IEEE Int. Conf. on Control Applications*, 2006, pp. 2890–2895.

[23] B. M. Anzel, "Method and apparatus for a satellite station keeping," U.S. Patent 5 443 231, August 22, 1995.

[24] N. Gopalswamy, J. M. Davila, F. Auchère, J. Schou, C. M. Korendyke, A. Shih, J. C. Johnston, R. J. MacDowall, M. Maksimovic, E. Sittler, *et al.*, "Earth-affecting solar causes observatory (easco): a mission at the sun-earth l5," in *SPIE Optical Engineering+ Applications*. Int. Society for Optics and Photonics, 2011, p. 81480Z.

[25] A. Verma, A. Fienga, J. Laskar, H. Manche, and M. Gastineau, "Use of messenger radioscience data to improve planetary ephemeris and to test general relativity," *Astronomy & Astrophysics*, vol. 561, p. A115, 2014.

[26] D. R. Stanbridge, K. E. Williams, A. H. Taylor, B. R. Page, C. G. Bryan, D. W. Dunham, P. Wolff, B. G. Williams, J. V. McAdams, and D. P. Moessner, "Achievable force model accuracies for messenger in mercury orbit," *Astrodynamics 2011, Adv. the Astronautical Sciences*, vol. 142, 2011.

[27] T. N. Edelbaum, "Optimum low-thrust rendezvous and station keeping," *AIAA Journal*, vol. 2, no. 7, pp. 1196–1201, 1964.

[28] A. Sukhanov and A. Prado, "On one approach to the optimization of low-thrust station keeping manoeuvres," *Adv. Space Research*, vol. 50, no. 11, pp. 1478–1488, 2012.

[29] V. M. Gomes and A. F. Prado, "Low-thrust out-of-plane orbital station-keeping maneuvers for satellites," *Mathematical Problems in Engineering*, vol. 2012, 2012.

[30] F. Topputo and F. Bernelli-Zazzera, "Optimal low-thrust stationkeeping of geostationary satellites," in *Proc. of Confederation of European Aerospace Societies Conf.*, 2011, pp. 1917–1925.

[31] D. Losa, "High vs low thrust station keeping maneuver planning for geostationary satellites," Ph.D. dissertation, École Nationale Supérieure des Mines de Paris, 2007.

[32] J. B. Rawlings and D. Q. Mayne, *Model predictive control: Theory and design*. Nob Hill Pub. Madison, Wisconsin, 2009.

[33] A. Walsh, S. Di Cairano, and A. Weiss, "MPC for coupled station keeping, attitude control, and momentum management of low-thrust geostationary satellites," in *Proc. American Control Conf.*, Boston, MA, 2016, pp. 7408–7413.

[34] D. Zlotnik, S. Di Cairano, and A. Weiss, "MPC for coupled station keeping, attitude control, and momentum management for GEO satellites using on-off electric propulsion," in *Proc. IEEE Conf. on Control Technology and Applications*, Kohala Coast, Hawai'i, 2017, pp. 1835–1840.

[35] R. L. Corey and D. J. Pidgeon, "Electric propulsion at space systems/loral," in *Proc. 31st Int. Electric Propulsion Conf., paper IEPC-2009-270*, 2009.

[36] D. A. Herman, "NASA's evolutionary xenon thruster (next) project qualification propellant throughput milestone: Performance, erosion, and thruster service life prediction after 450 kg," 2010.

[37] D. M. Goebel, J. E. Polk, I. Sandler, I. G. Mikellides, J. Brophy, W. G. Tighe, and K. Chien, "Evaluation of 25-cm xips© thruster life for deep space mission applications," in *Proc. 31st Int. Electric Propulsion Conf.*, Ann Arbor, MI, 2009.

[38] R. J. Caverly, S. Di Cairano, and A. Weiss, "Split-horizon MPC for coupled station keeping, attitude control, and momentum management of GEO satellites using on-off electric propulsion," in *Proc. American Control Conf.*, Milwaukee, WI, 2018, pp. 652–657.

[39] ——, "Quantization of an MPC policy for coupled station keeping, attitude control, and momentum management of GEO satellites," in *Proc. European Control Conf.*, Limassol, Cyprus, 2018, pp. 3114–3119.

[40] A. H. de Ruiter, C. Damaren, and J. R. Forbes, *Spacecraft dynamics and control: An introduction*. John Wiley & Sons, 2012.

[41] A. H. J. de Ruiter, C. J. Damaren, and J. R. Forbes, *Spacecraft Dynamics and Control: An Introduction*. Chichester, West Sussex, U.K.: John Wiley & Sons, Ltd, 2013.

[42] A. Weiss, I. Kolmanovsky, D. S. Bernstein, and A. Sanyal, "Inertia-free spacecraft attitude control using reaction wheels," *Jour. Guidance, Control, and Dynamics*, vol. 36, no. 5, pp. 1425–1439, 2013.

[43] A. Weiss, U. Kalabić, and S. Di Cairano, "Model predictive control for simultaneous station keeping and momentum management of low-thrust satellites," in *Proc. American Control Conf.*, Chicago, IL, 2015, pp. 2305–2310.

[44] A. H. J. de Ruiter, C. J. Damaren, and J. R. Forbes, *Spacecraft Dynamics and Control: An Introduction*. Chichester, West Sussex, UK: John Wiley & Sons, 2013.

[45] S. C. Wu, T. P. Yunck, S. M. Lichten, B. J. Haines, and R. P. Malla, "GPS-based precise tracking of Earth satellites from very low to geosynchronous orbits," in *Proc. Telesystems Conf.*, Washington, DC, 1992.

[46] T. Flohrer, H. Krag, and H. Klinkrad, "Assessment and categorization of TLE orbit errors for the US SNN catalogue," in *Proc. Advanced Maui Optical and Space Surveillance Technologies Conf.*, Maui, Hawai'i, 2008.

[47] Y. Hwang, B.-S. Lee, H.-Y. Kim, H. Kim, and J. Kim, "Orbit determination accuracy improvement for geostationary satellite with single station tracking data," *ETRI Journal*, vol. 30, no. 6, pp. 774–782, 2008.

[48] H. L. Fisher, M. D. Shuster, and T. E. Strikwerda, "Attitude determination for the star tracker mission," *Astrodynamics 1989*, pp. 139–150, 1990.

[49] S. Lee, G. G. Ortiz, and J. W. Alexander, "Star tracker-based acquisition, tracking, and pointing technology for deep-space optical communications," *Interplanetary Network Progress Report*, vol. 42, no. 161, pp. 201–214, 2005.

[50] W. Jiongqi, X. Kai, and Z. Haiyin, "Low-frequency periodic error identification and compensation for star tracker attitude measurement," *Chinese Jour. Aeronautics*, vol. 25, no. 4, pp. 615–621, 2012.

[51] M. Wang, C. Fan, B. Yang, S. Jin, and J. Pan, "On-ground processing of Yaogan-24 remote sensing satellite attitude data and verification using geometric field calibration," *Sensors*, vol. 16, no. 8, p. 1203, 2016.

[52] J. C. Springman and J. W. Cutler, "Flight results of a low-cost attitude determination system," *Acta Astronautica*, vol. 99, pp. 201–214, 2014.

[53] C. M. Pong, "High-precision pointing and attitude estimation and control algorithms for hardware-constrained spacecraft," Ph.D. dissertation, Massachusetts Institute of Technology, Cambridge, MA, 2014.

Ryan J. Caverly received the B.Eng. degree in mechanical engineering (Hons.) from McGill University, Montreal, QC, Canada, in 2013, and the M.Sc.Eng. and Ph.D. degrees in aerospace engineering from the University of Michigan, Ann Arbor, MI, USA, in 2015 and 2018, respectively.

He is currently an Assistant Professor of Aerospace Engineering & Mechanics at the University of Minnesota, Minneapolis, MN, USA. Prior to joining the University of Minnesota, he worked as an intern and then a consultant for Mitsubishi Electric Research Laboratories in Cambridge, MA, USA. His research interests include dynamic modeling and control systems, with a focus on robotic and aerospace applications.

Stefano Di Cairano (SM'15) received the Master's (Laurea) and the Ph.D. degrees in information engineering in 2004 and 2008, respectively, from the University of Siena, Italy. During 2008-2011, he was with Powertrain Control R&A, Ford Research and Advanced Engineering, Dearborn, MI, USA. Since 2011, he is with Mitsubishi Electric Research Laboratories, Cambridge, MA, USA, where he is currently a Distinguished Research Scientist, and the Senior Team Leader of Control for Autonomy. His research focuses on optimization-based control and decision-making strategies for complex mechatronic systems, in automotive, factory automation, transportation systems, and aerospace. His research interests include model predictive control, constrained control, path planning, hybrid systems, optimization, and particle filtering. He has authored/coauthored more than 150 peer-reviewed papers in journals and conference proceedings and has 35 patents.

Dr. Di Cairano was the Chair of the IEEE CSS Technical Committee on Automotive Controls and of the IEEE CSS Standing Committee on Standards. He is the inaugural Chair of the IEEE CCTA Editorial Board and was an Associate Editor of the IEEE TRANS. CONTROL SYSTEMS TECHNOLOGY.

Avishai Weiss is a Principal Research Scientist in the Control and Dynamical Systems group at Mitsubishi Electric Research Laboratories, Cambridge, MA. He received his Ph.D. in Aerospace Engineering in 2013 from the University of Michigan and holds B.S. and M.S. degrees from Stanford University in Electrical Engineering (2008) and Aeronautics and Astronautics (2009). His main research interests and contributions are in the areas of spacecraft orbital and attitude control, constrained control, model predictive control, and time-varying systems, in which he has authored over 45 peer-reviewed papers and patents.